Infrared and Raman spectra, conformational stability, ab initio calculations, and vibrational assignments for methylaminothiophosphoryl difluoride

ARTICLE *in* JOURNAL OF MOLECULAR STRUCTURE · JANUARY 2001

Impact Factor: 1.6 · DOI: 10.1016/S0022-2860(00)00759-6

ELSEVIER

Journal of Molecular Structure 560 (2001) 57–86

Journal of
MOLECULAR
STRUCTURE

www.elsevier.nl/locate/molstruc

Infrared and Raman spectra, conformational stability, ab initio calculations, and vibrational assignments for methylaminothiophosphoryl difluoride ☆

B.J. van der Veken[a], R.S. Sanders[a], J. Xiao[b], J.R. Durig[b,*]

[a]*Rijksuniversitair Centrum Antwerpen, 171 Groenenborgerlaan, Antwerpen 2020, Belgium*
[b]*Department of Chemistry, University of Missouri-Kansas City, Kansas City, MO 64110 USA*

Received 24 July 2000; accepted 21 August 2000

Abstract

Infrared spectra (4000–50 cm^{-1}) of the vapor, amorphous and crystalline solids and Raman spectra (3600–10 cm^{-1}) of the liquid with qualitative depolarization data as well as the amorphous and crystalline solids of methylaminothiophosphoryl difluoride, $CH_3N(H)P(=S)F_2$, and three deuterated species, $CD_3N(H)P(=S)F_2$, $CH_3N(D)P(=S)F_2$, and $CD_3N(D)P(=S)F_2$, have been recorded. The spectra indicate that in the vapor, liquid and amorphous solid a small amount of a second conformer is present, whereas only one conformer remains in the low temperature crystalline phase. The near-infrared spectra of the vapor confirms the existence of two conformers in the gas phase. Asymmetric top contour simulation of the vapor shows that the *trans* conformer is the predominant vapor phase conformer. From a temperature study of the Raman spectrum of the liquid the enthalpy difference between the *trans* and near-*cis* conformers was determined to be 368 ± 15 cm^{-1} (4.41 ± 0.2 kJ/mol), with the *trans* conformer being thermodynamically preferred. Ab Initio calculations with structure optimization using the 6-31G(d) and 6-311+G(d,p) basis sets at the restricted Hartree–Fock (RHF) and/or with full electron correlation by the perturbation method to second order (MP2) support the occurrence of near-*trans* (~5° from *trans*) and near-*cis* (~20° from *cis*) conformers. From the RHF/6-31G(d) calculation the near-*trans* conformer is predicted to be the more stable form by 451 cm^{-1} (5.35 kJ/mol) and from the MP2/6-311+G(d,p) calculation by 387 cm^{-1} (4.63 kJ/mol). All of the normal modes of the near-*trans* rotamer have been assigned based on infrared band contours, depolarization values and group frequencies and the assignment is supported by the normal coordinate calculation utilizing harmonic force constants from the MP2/6-31G(d) ab initio calculations.

Keywords: Infrared spectra; Raman spectra; Restricted Hartree–Fock

1. Introduction

For some time we have been investigating the conformational stability of a number of organophosphorus molecules [1–15]. For several of these molecules we have found that the more stable conformer is not the one that would be predicted from the '*gauche* effect' [16]. At this time, there does not appear to be any simple theory, which will correctly predict the more stable

☆ Taken in part from the thesis of R.S. Sanders which was submitted to the Department of Chemistry, University of Antwerp (Belgium), in partial fulfillment of the PhD degree and the thesis of J. Xiao, which will be submitted to the Department of Chemistry of the University of Missouri-Kansas City in partial fulfillment of the PhD degree.

* Corresponding author. Tel.: +1-816-235-1136; fax: +1-816-235-5502.

E-mail address: durigj@umkc.edu (J.R. Durig).

0022-2860/01/$ - see front matter
PII: S0022-2860(00)00759-6

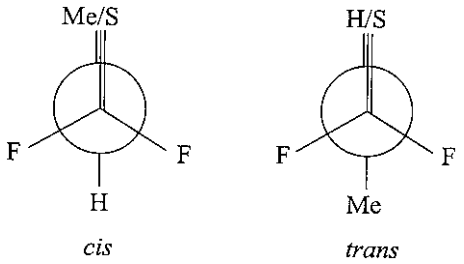

Fig. 1. The *cis* and *trans* conformers of methylaminothiophosphoryl difluoride.

conformer for these simple organophosphorus molecules. In order to provide additional information on the conformational stability of organophosphorus molecules a study of methylaminothiophosphoryl difluoride, $CH_3N(H)P(=S)F_2$ was initiated. There has been a previously reported [17] infrared study and, in this study, the mid-infrared spectra of the vapor phase (4000–600 cm^{-1}) and the solid (4000–350 cm^{-1}) were recorded. The authors concluded that the *cis* form (Fig. 1) is the more stable rotamer in the gas whereas they could not make a conformational assignment for the molecule in the solid state. In order to expand the vibrational and structural data available on this molecule and to obtain more conformational information we have recorded the infrared and Raman spectra of methyl aminothiophosphoryl difluoride and its three isotopomer derivatives, $CH_3N(D)P(=S)F_2$, $CD_3N(H)P(=S)F_2$ and $CD_3N(D)P(=S)F_2$, and have compared the data among the three physical states. Additionally, ab initio calculations using both the 6-31G(d) and 6-311+G(d,p) basis sets have been carried out at the restricted Hartree–Fock (RHF) and/or with full electron correlation by the perturbation method to second order (MP2) [18] to obtain the conformational stability, structural parameters, and fundamental frequencies for comparison to the experimental values. The results of this spectroscopic and theoretical study are reported herein.

2. Experimental

Methylaminothiophosphoryl difluoride, $CH_3N(H)P(=S)F_2$, was prepared according to the procedure of. Cavell et al. [17]. This method is based on the vapor phase reaction of methylamine with chlorothiophosphoryldifluoride (2:1 molar ratio). These compounds were mixed and after a reaction time of one to two hours, the mixture was transferred to a low temperature, low pressure fractional distillation column for purification. The isotopic species were prepared in the same manner by using CH_3ND_2, CD_3NH_2 or CD_3ND_2 as the starting materials. Methylamine-d_3 was obtained by the reaction of CD_3NH_2HCl (Janssen Chimica) with NaOH in H_2O solution. Methylamine-d_2 and methylamine-d_5 were prepared by several successive exchanges of methylamine and methylamine-d_3, respectively, with concentrated NaOD in D_2O solution. The different isotopic methylamines were purified by vacuum distillation and checked for isotopic purity by their vapor phase infrared spectra. Chlorothiophosphoryldifluoride was prepared by partial fluorination of thiophosphoryl trichloride with freshly sublimed antimony trifluoride (Janssen Chimica), followed by vacuum fractionation.

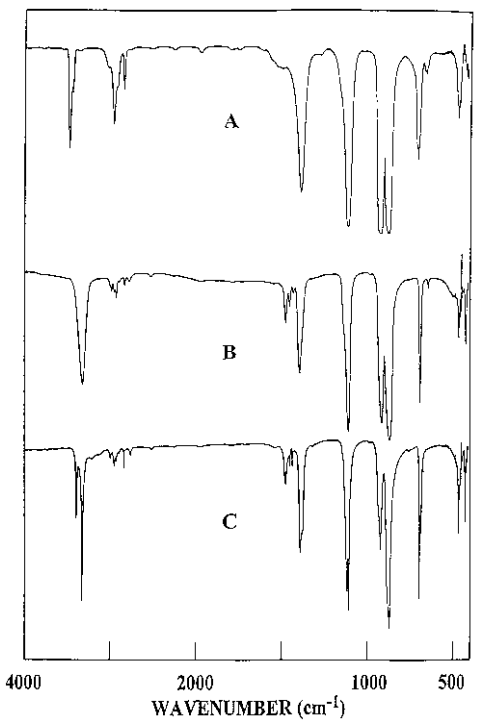

Fig. 2. Mid infrared spectra of gaseous (A); amorphous solid (B); and crystalline solid (C) $CH_3N(H)P(S)F_2$.

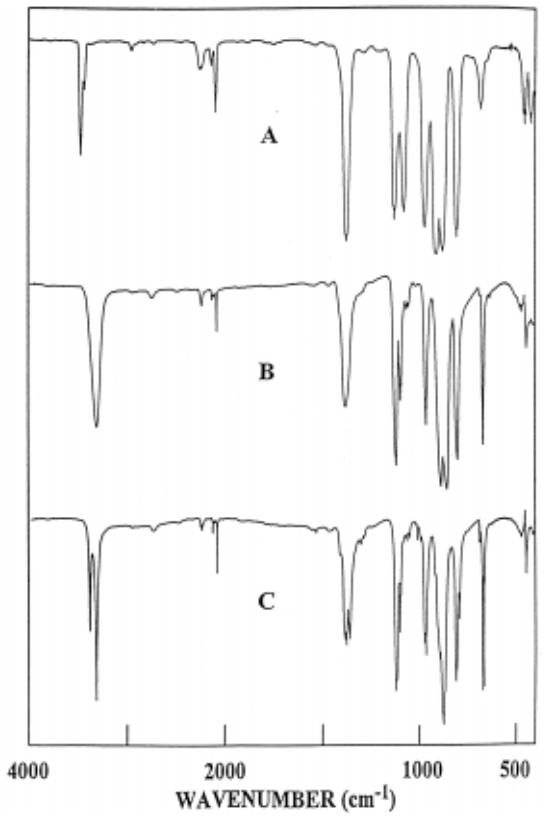

Fig. 3. Mid infrared spectra of gaseous (A); amorphous solid (B); and crystalline solid (C) $CD_3N(H)P(S)F_2$.

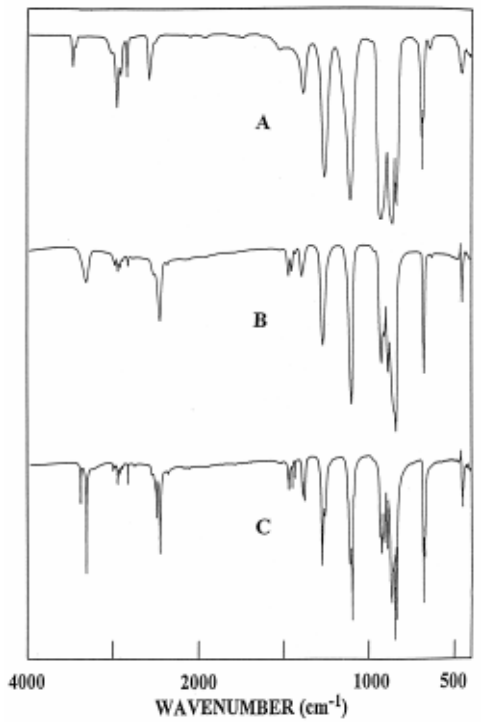

Fig. 4. Mid infrared spectra of gaseous (A); amorphous solid (B); and crystalline solid (C) $CH_3N(D)P(S)F_2$.

The mid-infrared spectra (Figs. 2–5) of the vapors were obtained on a Bruker model IFS 113v Fourier transform spectrometer equipped with a Ge/KBr beamsplitter, a Globar source and a broad band MCT detector. The spectra were recorded at a different vapor pressure up to 10 mbar in a 30 cm cell fitted with KBr windows. The interferograms were recorded 250 times with a resolution of 0.5 cm^{-1} and transformed with a Happ–Genzel apodization function. The corresponding spectra of the solids were recorded on the same instrument by condensing the samples on a CsI plate held at boiling liquid nitrogen temperature. The amorphous samples obtained in this way were annealed until no further changes in the spectra were observed.

The far-infrared spectra (Figs. 6–9) of the solids were obtained by condensing the compound from the vapor onto a cooled Si-window, using the Bruker model IFS 113v spectrometer equipped with Mylar beamsplitters, a Globar source, a DTGS detector and a liquid helium cooled Si bolometer. A total of 100 interferograms were co-added and Happ–Genzel apodized so as to obtain a resolution of 0.5 cm^{-1}. The far-infrared spectra of the vapors were obtained on this same instrument with the sample contained in a 30 cm cell equipped with polyethylene windows. The spectral data were treated the same as for the solid.

The Raman spectra (3600–10 cm^{-1}) (Figs. 10–13) were recorded on a SPEX model 1403 Raman spectrometer equipped with a Spectra-Physics model 2020 argon ion laser operating on the 514.5 nm line. The laser power at the samples was varied from 0.5 to 1.5 W depending on the physical state under investigation. The spectra of the liquids were obtained from the samples sealed in a glass capillary, and variable temperature experiments in this phase were carried out in a Miller–Harney cell [19]. The solid samples

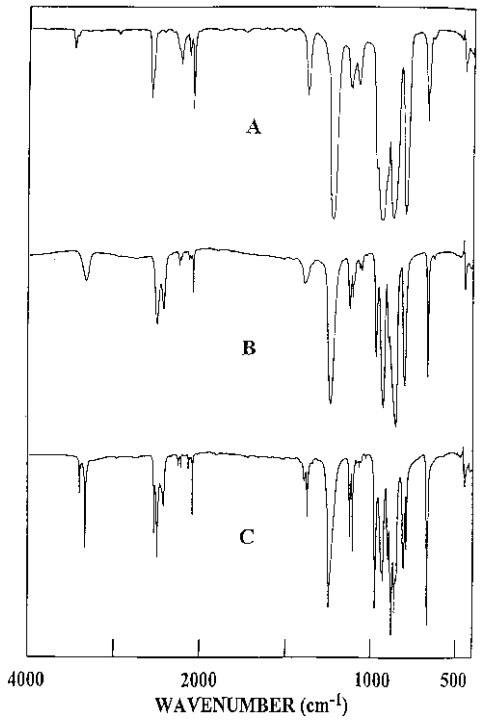

Fig. 5. Mid infrared spectra of gaseous (A); amorphous solid (B); and crystalline solid (C) $CD_3N(D)P(S)F_2$.

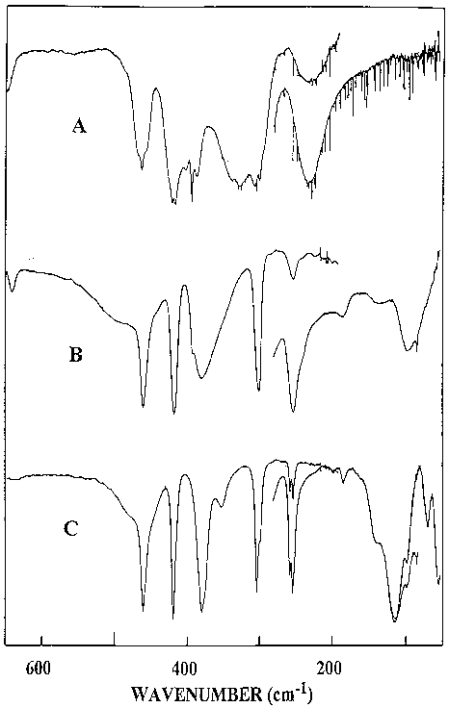

Fig. 6. Far infrared spectra of gaseous (A); amorphous solid (B); and crystalline solid (C) $CH_3N(H)P(S)F_2$.

were obtained by condensation from the liquids (in a sealed glass capillary) and annealing, using a Miller–Harney cell, or by condensing the samples onto a blackened brass block maintained at about 77 K by boiling liquid nitrogen. Depolarization measurements were made with the standard SPEX accessories. The spectra were measured with a resolution of 2.0 cm^{-1}. Because of the relatively low vapor pressure of the compounds, no vapor phase Raman spectra could be recorded. The observed infrared and Raman bands are listed in Tables 1–4.

The near-infrared spectra of the vapor phase were also recorded with the Bruker IFS 113v spectrometer, equipped with a Si/CaF_2 beamsplitter, a Globar source and a broad band MCT detector. For the gas phase the sample was examined by using the maximum vapor pressure of approximately 10 mbar in a 10 m cell fitted with quartz windows. Interferograms were recorded 1000 times with a resolution of 0.5 cm^{-1} and transformed with a Happ–Genzel apodization function.

3. Ab initio calculations

Because there are no previously reported experimental data with regard to the structure of methylaminothiophosphoryl difluoride, the initial molecular structure was determined by ab initio calculations. The ab initio calculations were made with the program GAUSSIAN-98 [20] at the restricted Hartree–Fock (RHF) level and with full electron correlation (second order Moller–Plesset perturbation theory) using Gaussian type basis functions with the 6-31G(d) and/or 6-311+G(d,p) basis sets. Density function theory (DFT) calculations were also made with GAUSSIAN-98 [20], which were restricted to the hybrid B3LYP method with the 6-31G(d) basis set. The energy minima with respect to the nuclear coordinates were obtained by the simultaneous relaxation of all the geometric parameters using the gradient method of Pulay [21]. All the calculations converged on the near-*trans* and near-*cis* conformers, instead of the perfect *trans* and *cis* conformer (Fig. 1). The

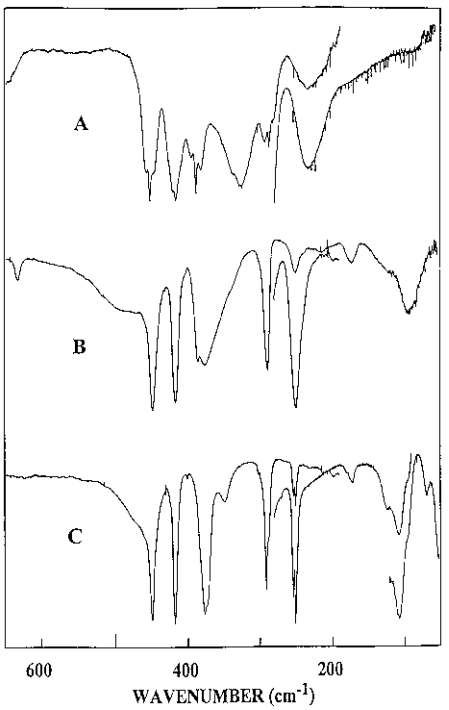

Fig. 7. Mid infrared spectra of gaseous (A); amorphous solid (B); and crystalline solid (C) $CD_3N(H)P(S)F_2$.

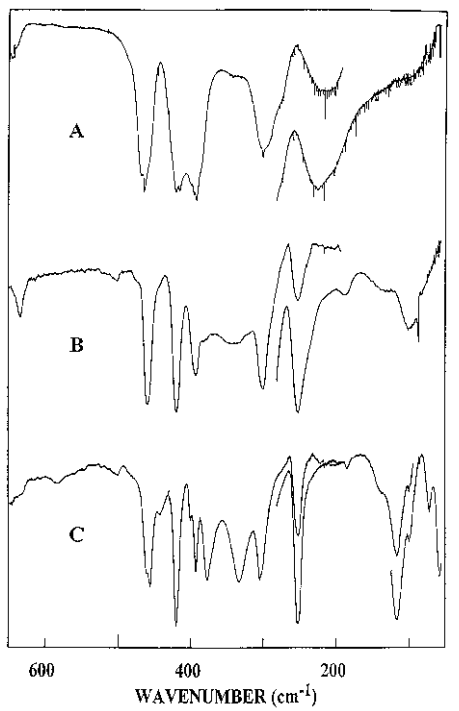

Fig. 8. Mid infrared spectra of gaseous (A); amorphous solid (B); and crystalline solid (C) $CH_3N(D)P(S)F_2$.

structural parameters as determined with these calculations are given in Table 5 for both conformations. It should be noted that for the near-*trans* conformer, the dihedral angle SPNC ranged from 172.8° from the MP2/6-31G(d) calculation to 174.8° from the RHF/6-31G(d) calculation. Such a small dihedral angle away from the planar structure makes this conformer effectively *trans* in the spectroscopic study. In order to assist our experimental study, calculations were carried with the SPNC dihedral angle fixed at 180°. The force fields which resulted were utilized for the normal coordinate analysis stated below.

In order to obtain a more complete description of the molecular motions involved in the normal modes, we have also carried out a normal coordinate analysis. This analysis was performed utilizing ab initio calculations and the classic Wilson GF matrix method [22] with the computer programs written by Schachtschneider [23]. The force fields in Cartesian coordinates were calculated by the GAUSSIAN-98 program [20] with the MP2/6-31G(d) basis set. Internal coordinates (Fig. 14) were used to calculate the B matrix and using this B matrix, the force field in Cartesian coordinates was then converted to the force field in internal coordinates [24]. The resulting force field can be obtained from the authors. Initially, all scaling factors were kept fixed at a value of 1.0 to reproduce the pure ab initio calculated vibrational frequencies. Subsequently, scaling factors of 0.88 for carbon–hydrogen stretches, 0.90 for carbon–hydrogen bends, heavy atom stretches and methyl torsions and 1.0 for heavy atom bends and asymmetric torsion, and the geometric average of scaling factors for interaction force constants were used to obtain the fixed scaled force field and resultant wavenumbers. A set of symmetry coordinates were used (Table 6) to determine the corresponding potential energy distributions (PEDs). A comparison between the observed and calculated infrared intensities, Raman activities, depolarization ratios and PEDs are given in Tables 7–10.

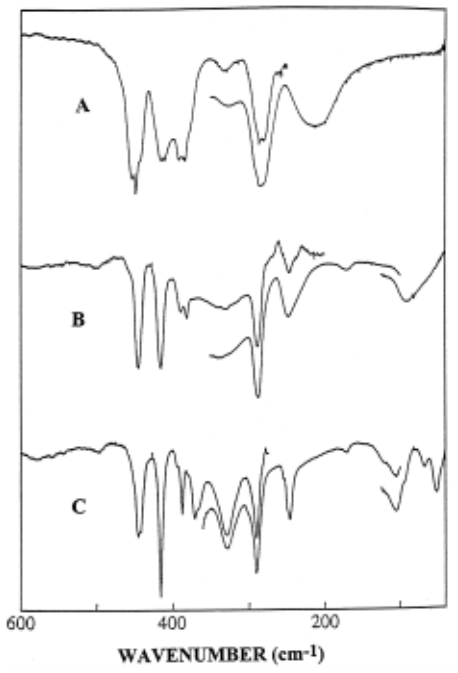

Fig. 9. Mid infrared spectra of gaseous (A); amorphous solid (B); and crystalline solid (C) $CD_3N(D)P(S)F_2$.

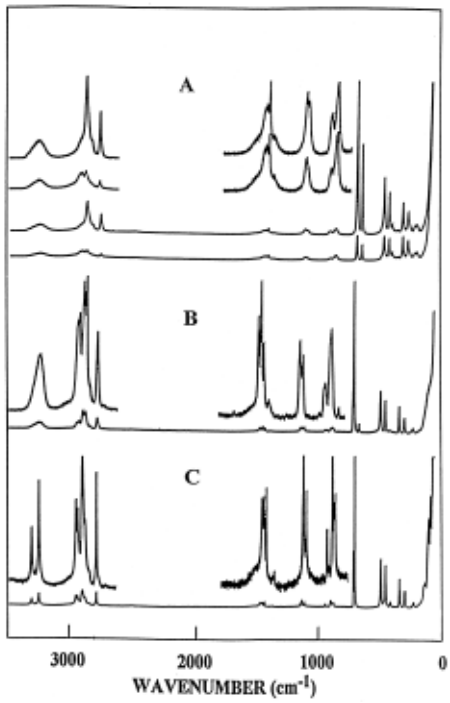

Fig. 10. Raman spectra of liquid (A); amorphous solid (B); and crystalline solid (C) $CH_3N(H)P(S)F_2$.

4. Conformational analysis and stability

As suggested by the ab initio calculations, we can expect the existence of two conformers, the near-*cis* and *trans* rotamers, in the fluid phases. The vapor phase infrared spectra (Figs. 2–5) of the four isotopic derivatives indeed show the appearance of a weaker second band in the PS stretching region, which can only be assigned to a second conformer. This is clearly substantiated by the low temperature study where the PS stretch of the second conformer disappears upon crystallization, for each of the four isotopic species investigated.

As will be shown below, ν(NH) and ν(ND) are observed as a doublet in the fluid phases of each of the isotopic derivatives. If this doublet structure were due to Fermi resonance, it is unlikely that the first overtone of ν(NH) and ν(ND) would give rise to a similar doublet structure. In Fig. 15, the fundamental and the first overtone of ν(NH) in the infrared spectrum of the d_0 vapor are shown. It is clear that the first overtone also occurs as a doublet. A very similar pattern is observed for the first overtone of ν(NH) in the d_3 isotopomer, and in that of ν(ND) in d_1 molecule. Therefore, we conclude that the doublet structure is not due to Fermi resonance, but is due to the presence of a second conformer. In contrast to the patterns observed for d_0, d_1 and d_3, the first overtone of ν(ND) in d_4 shows a triplet structure. Hence, in one or both conformers this vibration must be in Fermi resonance with another overtone. No attempts were made to give a detailed assignment of these three transitions.

In a series of papers [6–8,10–12] we have shown that infrared band contour simulation can be used to identify the conformers present in the gaseous state. The a priori knowledge of the orientation of a $\partial\mu/\partial Q$ for the simulation of gas phase contours restricts the fundamentals that can be used to those that are sufficiently characteristic, whereas also the contours calculated for the proposed conformers must differ sufficiently from each other to allow for conclusive conformational results to be drawn.

For the present compound, ν(NH) and ν(ND) are

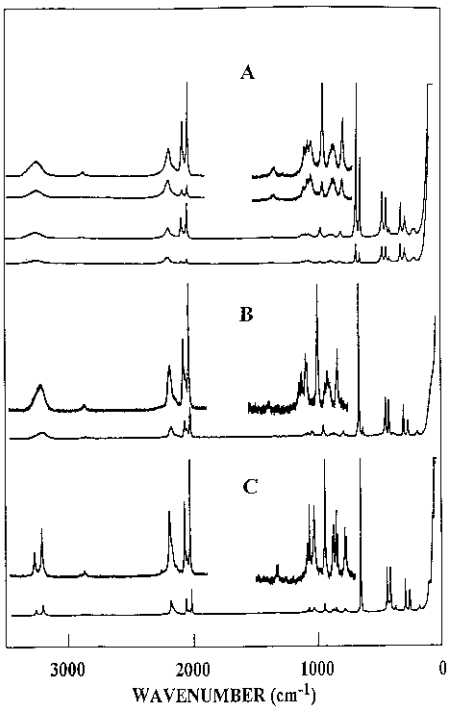

Fig. 11. Raman spectra of liquid (A); amorphous solid (B); and crystalline solid (C) $CD_3N(H)P(S)F_2$.

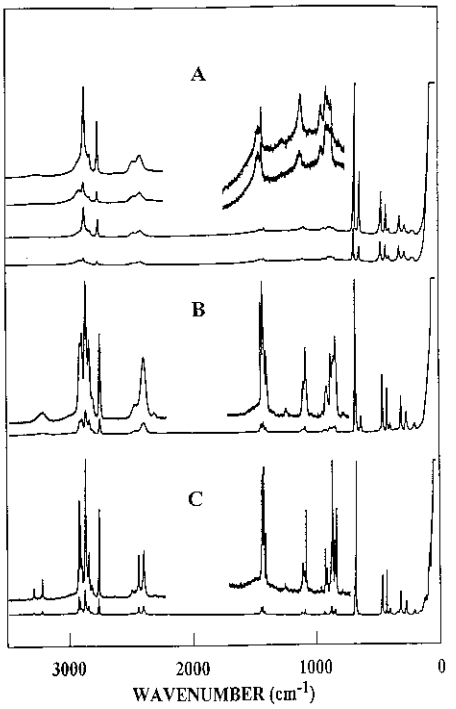

Fig. 12. Raman spectra of liquid (A); amorphous solid (B); and crystalline solid (C) $CH_3N(D)P(S)F_2$.

highly characteristic vibrations. However, the contours observed experimentally for these vibrations are strongly thermally broadened, so that their P, Q and R structure has almost completely disappeared. Therefore, these contours cannot be used to abstract conformational information. In addition to not showing conformational splitting, $\nu(CH_3)$ is also found to be in strong Fermi resonance. Both phenomena are indications against the use of the $\nu_s(CH_3)$ contour in simulations. Of the other fundamentals, only ν(P=S) shows a well defined conformer doublet (vide infra). Hence this vibration, which has been successfully used in simulations before [11], was selected.

The pure type A, B and C infrared contours of the *trans* conformers of $CH_3N(H)P(=S)F_2$ and its d_1, d_3 and d_4 isotopomers were calculated using the rotational constants obtained from the microwave data [25]. Those for the near-*cis* conformer were calculated using the rotational constants obtained by assuming for the near-*cis* conformer the bond lengths and valency angles from Table 5. All pure type contours were calculated to a maximum J level of 150, using a slit of 0.5 cm^{-1}. With the assumption that the direction of $\partial\mu/\partial Q$ for the ν(P=S) fundamental is parallel to the P=S bond, the directional cosines for $\partial\mu/\partial Q$ in the principal axis system were calculated. These are given in Table 11. The directional cosines were used to obtain the hybrid contours for the corresponding fundamentals as described earlier [26]. Additional convolutions, with Gaussian or Lorentzian functions, of the theoretical hybrids were necessary to account for thermal effects. The reproduction of the full width at half height of the Q branch was used as a criterion for the slit width used in the additional convolutions. As can be seen from Table 11, the ν(P=S) contour for the *trans* conformer is almost pure type A, whereas the hybrid for the *cis* conformer is expected to show an appreciable amount of B type character.

In Fig. 16 the experimental contour of the ν(P=S) doublet (B) is compared to the contours simulated with the high frequency component assigned to either

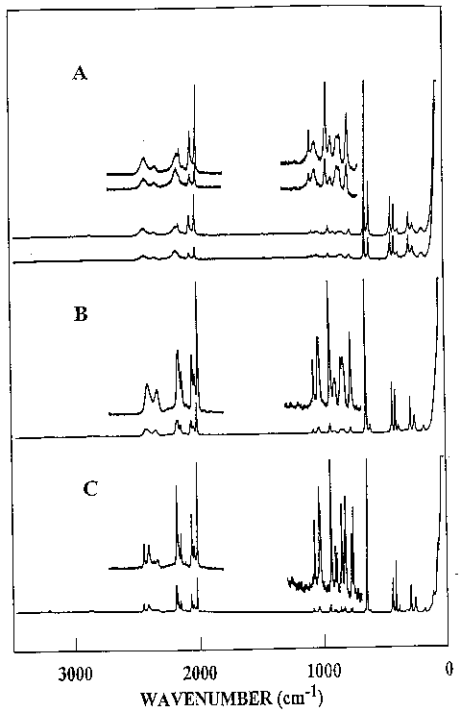

Fig. 13. Raman spectra of liquid (A); amorphous solid (B); and crystalline solid (C) $CD_3N(D)P(S)F_2$.

the near-*cis* conformer (A) or the *trans* conformer (C) and vice versa for the low frequency component. It is clear that from the simulation of the low frequency component no conclusion can be drawn. However, the simulation of the high frequency component with the near-*cis* hybrid leads to a split Q branch, clearly absent in the experimental contour. The agreement of the experimental high frequency contour with the one simulated using the *trans* conformer confirms that the intense high frequency ν(P=S) component must be due to the *trans* conformer. A similar result is obtained from the simulations of the ν(P=S) doublet in the d_3 molecule.

In Fig. 17 the experimental contour of the ν(P=S) doublet in the d_1 derivative (B) is compared to the contours simulated with the high frequency component assigned to the near-*cis* (A) or the *trans* (D) rotamer. It is clear again that simulation A is to be rejected. Simulation D, however, does not reproduce the asymmetry in the P and R branch of the experimental high frequency component. As the same asymmetry is not observed in the d_0 compound, it is unlikely to be due to anharmonicity of the ν(P=S). From the infrared spectra of the d_1 molecule it can be seen, however, that this compound contains an appreciable amount of the d_0 compound as isotopic impurity. The latter shows its ν(P=S) vibrations only slightly shifted from those in the d_1 compound. By admixing an amount of contour C of Fig. 16, at the correct frequencies, to account for the isotopic impurity, the observed asymmetry is reproduced, as is shown by contour C of Fig. 17. Also, in this way the low frequency component is correctly reproduced, confirming the origin of the phenomena.

In order to determine the enthalpy difference between the *trans* and near-*cis* conformers, a variable temperature Raman study of the liquid phase was undertaken utilizing an experimental technique similar to that described by Miller and Harney [19]. As can be seen from the Raman spectra in Fig. 18, the lines assigned to the PS stretch of the *trans* and near-*cis* conformers show significant intensity changes upon cooling. Since these lines are very strong and well separated from each other and from other lines, they were selected for the temperature study.

For each of the isotopes at a series of temperatures between 77 and −138°C, this doublet was recorded (Table 12). A least squares curve fitting of these spectra, using Gauss/Lorentz sum bands to fit the observed curves, allowed the relative intensities of the two bands to be expressed as band areas. From these data, ΔH was found to be $354 \pm 13\ cm^{-1}$ (4.24 ± 0.16 kJ/mol) in d_0, $404 \pm 18\ cm^{-1}$ (4.83 ± 0.22 kJ/mol) in d_3, $369 \pm 15\ cm^{-1}$ (4.42 ± 0.18 kJ/mol) in d_1 and $368 \pm 19\ cm^{-1}$ (4.40 ± 0.23 kJ/mol) in the d_4 derivative. The average value of $368 \pm 15\ cm^{-1}$ (4.41 ± 0.18 kJ/mol) clearly indicates that the *trans* conformer is the more stable form in the liquid state.

Assuming the absorption coefficient for ν(P=S) to have comparable values in both conformers, and making the usual assumption of a negligible entropy difference between the *trans* and near-*cis* conformer, the vapor phase infrared relative intensities of the ν(P=S) doublet suggest that in the vapor phase the *trans* conformer is even more stable relative to the *cis* than in the liquid phase. The Raman spectrum of the crystalline solid is also

Table 1
Observed infrared and Raman frequencies (cm^{-1}) and vibrational assignments for $CH_3N(H)P(S)F_2$ (abbreviations used: v, very; s, strong; m, moderate; w, weak; br, broad; sh, shoulder; p, polarized; R, Q and P refer to band contours in the gas phase infrared spectrum)

Infrared						Raman							Assignments
Gas	Rel. int.	Amorphous	Rel. int.	Crystalline	Rel. int.	Liquid	Rel. int.	Amorphous	Rel. int.	Crystalline	Rel. int.	ν_i[a]	
				3397	w								crystal effect
				3391	w					3390	vw		crystal effect
3480	m	3328	s	3325	m	3352	p,br vw	3332	vw	3328	w	ν_1	NH stretch
3446	vw											ν'_1	NH stretch (near-*cis*)
3023	vw			3013	vw					3012	vw	ν_2	CH_3 antisymmetric stretch
		2989	vw	2999	vw	2993	sh	2992	w	3000	vw	ν_{16}	CH_3 antisymmetric stretch
2963	m	2957	vw	2956	vw	2956	p m	2956	w	2960	w	ν_3	CH_3 symmetric stretch
2925	vw	2934	w	2936	vw			2936	w	2939	vw		
		2900	vw			2909	sh						
2852 R													
2847 Q	w	2840	vw	2843	vw	2844	p w	2841	w	2844	w		Fermi resonance
2842 P													
		1478	m	1477	w	1470	sh	1478	vw	1475	vw	ν_4	CH_3 antisymmetric deformation
		1454	w	1452	vw	1460	vw	1454	vw	1457	vw	ν_{17}	CH_3 antisymmetric deformation
		1433	vw	1438	vw	1436	p vw	1436	vw	1439	vw	ν_5	CH_3 symmetric deformation
				1394	vw								crystal effect
1391	s	1397	s	1389	m	1394	vw	1399	vw	1373	vw	ν_6	NH deformation
				1376	vw								crystal effect
1160	sh	1138	sh	1126	s	1124	p w	1129	vw	1130	sh	ν_8	CN stretch
										1124	vw	ν_{18}	CH_3 out-of-plane rock
1113	vs	1110	vs	1105	s	1107	p vw	1102	vw	1102	vw	ν_7	CH_3 rock
				934	sh								
923	vs	911	vs	915	m	913	p w	914	vw	927	vw	ν_9	PF_2 symmetric stretch
877	vs			878	sh					881	vw	ν_{19}	PF_2 antisymmetric stretch
867	sh	865	vs	863	vs	866	p w	867	vw	867	vw	ν_{10}	NP stretch
704 R													
699 Q	m	686	s	684	s	684	p vs	679	vs	687	m	ν_{11}	PS stretch
695 P				680	m					675	vs		
				677	m								
657 R													
651 Q	w	638	w			640	p s	638	vw			ν'_{11}	PS stretch (near-*cis*)
645 P													
		500	sh br	500	sh bv							ν_{21}	NH out-of-plane bend
465 R													
461 Q	vs	458	vs	458	vs	457	p s	456	m	455	m	ν_{12}	PF_2 wag

Table 1 (*continued*)

Infrared						Raman							Assignments
Gas	Rel. int.	Amorphous	Rel. int.	Crystalline	Rel. int.	Liquid	Rel. int.	Amorphous	Rel. int.	Crystalline	Rel. int.	ν_i[a]	
456 P													
440	sh	440	vw									ν'_{14}	CNP bend (near-*cis*)
418 Q													
414 Q	vs	416	vs	417	vs	415	p m	416	m	417	m	ν_{20}	PF_2 rock
400 R													
392Q	vs	390	s			389	vw	391	vw			ν'_{13}	PF_2 symmetric deformation (near-*cis*)
385 P													
				378	vs					376	vw	ν_{13}	PF_2 symmetric deformation
		348	sh	350	m	345	vw					ν_{21}	NH out-of-plane bend
336 R													
325 Q	w											ν'_{20}	PF_2 rock (near-*cis*)
305 R													
299 Q	w	300	s	302	s	299	p m	301	m	302	w	ν_{14}	CNP bend
				298	sh					297	w		
				257	m					257	w		crystal effect
242 br	vw	253	vw	253	m	254	w	255	w	252	w	ν_{22}	PF_2 twist
233 br	vw	240	sh									ν'_{22}	PF_2 twist (near-*cis*)
						194	vw					ν'_{15}	NPS bend (near-*cis*)
		180	vw	180	vw	182	vw	182	vw	180	vw	ν_{15}	NPS bend
				135	w							ν_{23}	CH_3 torsion
		95	vw	112	m					92	vw	ν_{24}	asymmetric torsion
				95	w					81	vw		
				66	w								
				52	m					49	s		lattice modes
										34	s		

[a] ν_i' refer to the near-*cis* conformer.

Table 2
Observed infrared and Raman frequencies (cm^{-1}) and assignments for $CD_3N(H)P(S)F_2$ (abbreviations used: v, very; S, strong; m, moderate; w, weak; br, broad; sh, shoulder; p, polarized; R, Q and P refer to band contours in the gas phase infrared spectrum)

Infrared						Raman							Assignments
Gas	Rel. int.	Amorphous	Rel. int.	Crystalline	Rel. int.	Liquid	Rel. int.	Amorphous	Rel. int.	Crystalline	Rel. int.	ν_i[a]	
				3393	m					3391	vw		crystal effect
3482	m	3328	s	3318	vs	3357	p brw	3333	br w	3330	vw	ν_1	NH stretch
3447	vw											ν_1	NH stretch (near-*cis*)
										3013	vw		
										2991	vw		
2968	vw					2965	p vw	2968	vw	2972	vw		
2925	vw												
2852 R													
2847 Q	vw					2841	p vw			2845	vw		
2842 P													
2265	w	2260	sh	2261	vw			2255	sh	2261	w	ν_2	CD_3 antisymmetric stretch
				2253	vw					2253	vw		
2241	vw	2243	vw	2243	vw	2241	br w	2249	w	2243	vw	ν_{16}	CD_3 antisymmetric stretch
				2226	vw								
				2206	sh					2206	vw		
2140	w	2133	vw	2133	vw	2133	p w	2132	w	2133	w		Fermi resonance
		2113	ww	2114	vw			2113	vw	2112	vw		
2093	m	2085	w	2087	w	2087	p m	2085	m	2087	w	ν_3	CD_3 symmetric stretch
				1388	m								crystal effect
1382	vs	1388	m	1380	m	1374	vw	1377	vw	1377	vw	ν_6	NH deformation
				1364	m					1362	vw		crystal effect
1138 R													
1133 Q	s	1124	s	1125	s	1119 p,	vw	1121	vw	1118	vw	ν_5	CD_3 symmetric deformation
1127 P				1120	sh								
1082	s	1098	m	1102	m	1093	vw	1101	vw	1100	vw	$\nu_4\nu_8$	CD_3 antisymmetric deformation, CN stretch
		1066	vw	1065	vw	1063	vw	1064	vw	1061	vw	ν_{17}	CD_3 antisymmetric deformation
		1054	vw					1056	sh			ν'_{17},ν'_5	CD_3 symmetric deformation (near-*cis*)
													CD_3 antisymmetric deformation (near-*cis*)
				973	m								
973	s	966	m	965	m	967	p w	966	vw	969	w	ν_7	CD_3 rock
										905	vw		
913	vs	887	vs	891	w	905	sh	914	sh	893	vw	ν_9	PF_2 symmetric stretch
876	vs	857	vs	874	vs	877	br vw	881	vw	874	vw	ν_{19}	PF_2 antisymmetric stretch
								864	sh	859	vw	ν_{18}	CD_3 out-of-plane rock

Table 2 (*continued*)

Infrared						Raman							Assignments
Gas	Rel. int.	Amorphous	Rel. int.	Crystalline	Rel. int.	Liquid	Rel. int.	Amorphous	Rel. int.	Crystalline	Rel. int.	ν_i[a]	
810 R													
805 Q	vs	802	s	808	s	795	p vw	796	vw	803	vw	ν_{10}	NP stretch
800 P													
				791	m					789	vw		crystal effect
		685	ww	687	vw					686	vw		PS stretch (Isotopic impurity)
				681	vw					681	vw		crystal effect
				670	s					669	s		crystal effect
680 R													
677 Q	m	667	s	662	s	667	p vs	664	vs	662	vs	ν_{11}	PS stretch
646	vw	632	vw			634	p s	632	vw			ν_{11}	PS Stretch (near-*cis*)
454 R													
		480	sh br	480	sh br							ν_{21}	ND out-of-plane bend
449 Q	s	446	vs	446	vs	445	p m	443	m	445	m	ν_{12}	PF_2 wag
444 P													
417 Q													
414 Q	vs	415	vs	416	vs	414	p m	415	rn	416	m	ν_{20}	PF_2 rock
392 R													
386 Q	vs	383	m			389	vw	383	vw			ν'_{13}	PF_2 symmetric deformation (near-*cis*)
380 P													
				375	vs					373	vw	ν_{13}	PF_2 symmetric deformation
336 Q	vs	343	s	347	w	333	vw					ν_{21}	NH out-of-plane bend
328 P													
294 R													
288 Q	vs	289	vs	291	s	288	p m	289	m	291	m	ν_{14}	CNP bend
281 P													
				254	w					254	w		crystal effect
250	sh br	250	w	251	w	253	w	253	w	250	sh	ν_{22}	PF_2 twist
233	m											ν'_{22}	PF_2 twist (near-*cis*)
						181	vw					ν'_{15}	NPS bend (near-*cis*)
		172	vw	170	ww	171	vw	171	vw	169	vw	ν_{15}	NPS bend
				122	m							ν_{23}	CD_3 torsion
		94	vw	106	s					90	vw	ν_{24}	asymmetric torsion
				69	w					77	vw		Lattice modes
				51	m					48	m		
										34	m		

[a] ν_i' refer to the near-*cis* conformer.

Table 3
Observed infrared and Raman frequencies (cm^{-1}) and assignments for $CH_3N(D)P(S)F_2$ (abbreviations used: v, very; s, strong; m, moderate; w, weak; br, broad; sh, shoulder; p, polarized; R, Q and P refer to band contours in the gas phase infrared spectrum)

Infrared						Raman						Assignments	
Gas	Rel. int.	Amorphous	Rel. int.	Crystalline	Rel. int.	Liquid	Rel. int.	Amorphous	Rel. int.	Crystalline	Rel. int.	ν_i [a]	
				3395	w					3395	vw		crystal effect (d_0)
3481	w	3325	w	3325	m	3350	p	3325	vw	3325	vw		NH stretch (d_0)
3446	vw												NH stretch (d_0, near-*cis*)
3024	vw	3010	sh	3014	vw					3015	w	ν_2	CH_3 antisymmetric stretch
				2999	vw	2990	sh	2892	vw	3000	vw	ν_{16}	CH_3 antisymmetric stretch
		2990	vw	2990	vw					2992	vw		
2965	m	2957	vw	2962	vw	2958	p w	2957	w	2963	w	ν_3	CH_3 symmetric stretch
				2956	sh								
2921	w	2927	vw	2935	vw			2929	vw	2931	vw		
		2902	vw	2906	vw	2909	vw	2905	vw	2906	vw		
2853 R													
2848 Q	w	2839	vw	2846	vw	2842	p w	2841	w	2847	w		Fermi resonance
2842 P													
				2843	vw								
				2564	vw					2562	vw		crystal effect
		2534	vw			2537	p w	2539	vw				Fermi resonance
				2511	w					2510	vw		crystal effect
2588	w	2468	m	2468	m	2480	p w	2470	w	2467	vw	ν_1	ND stretch
2562	sh											ν'_1	ND stretch (near-*cis*)
2510	vw												
		2377	vw										
		1474	w	1474	vw			1473	vw	1474	vw	ν_4	CH_3 antisymmetric deformation
		1454	w	1453	vw	1460	vw	1457	vw	1459	vw	ν_{17}	CH_3 antisymmetric deformation
		1435	vw	1439	vw	1437	p vw	1440	vw	1435	vw	ν_5	CH_3 symmetric deformation
				1395	w								crystal effect (d_0)
				1387	w								crystal effect (d_0)
1392	rn	1398	w	1382	w								NH deformation (d_0)
1265	s	1276	m	1280	m	1265	p vw	1265	vw	1277	vw	ν_8	CN stretch
				1264	w					1263	vw		crystal effect
1140	sh					1130	p vw	1124	vw	1130	vw	ν_8	CN stretch (d_0)
1116	s	1108	vs	1117	m	1113	sh			1117	vw	ν_7	CH_3 rock
				1105	vs			1101	vw	1100	vw	ν_{18}	CH_3 out-of-plane rock
942 Q	vs	932	s	933	m	932	vw	931	vw	939	vw	ν_9	PF_2 symmetric stretch
932 Q													
		914	m	917	m					925	vw		PF_2 symmetric stretch (d_0)
				898	m					899	vw		

Table 3 (*continued*)

Infrared						Raman							Assignments
Gas	Rel. int.	Amorphous	Rel. int.	Crystalline	Rel. int.	Liquid	Rel. int.	Amorphous	Rel. int.	Crystalline	Rel. int.	ν_i[a]	
		893	s	888	m	890	vw	894	vw	890	vw		
878	vs	864	sh	868	s	870	ww	868	sh	878	vw	ν_6	ND deformation
										861	vw		
850 Q				853	vs					854	vw	ν_{19}	PF_2 antisymmetric stretch
844 Q	s	842	vs	843	vs	847	vw	847	vw	845	vw	ν_{10}	NP stretch
				687	m								
				683	s					683	rn		crystal effect
698 R													
692 Q	s	682	s	678	m	680	p vs	675	vs	673	vs	ν_{11}	PS stretch
687 P													
651 Q													
643 Q	vw	632	vw			635	p s	632	w			ν'_{11}	PS stretch (near-*cis*)
465 Q													
462 Q	vs	457	vs	455	s	456	p rn	454	m	452	m	ν_{12}	PF_2 wag
417 Q													
412 Q	vs	417	vs	417	vs	415	p rn	416	rn	417	m	ν_{13}	PF_2 symmetric deformation
396 R													
393 Q	vs											ν'_{20}	PF_2 rock (near-*cis*)
389 Q		390	s	390	s	387	vw	391	vw	389	vw	ν_{21}	ND out-of-plane bend
				375	s					374	vw	ν_{20}	PF_2 rock
340	vw	340	w	332	s					323	vw	ν_{21}	ND out-of-plane bend
300	m	299	s	303	s	300	m	300	m	301	w	ν_{14}	CNP bend
280	sh	280	vw									ν'_{21}	ND out-of-plane bend (near-*cis*)
		250	w	250	m	254	w	256	w	251	w	ν_{22}	PF_2 twist
223	w	230	sh									ν'_{22}	PF_2 twist (near-*cis*)
						193	vw					ν'_{15}	NPS bend (near-*cis*)
		180	vw	182	vw	181	vw	182	vw	178	vw	ν_{15}	NPS bend
				135	sh					130	sh	ν_{23}	CH_3 torsion
		95	vw	112	m					95	vw	ν_{24}	Asymmetric torsion
				95	vw								
				67	w					82	vw		
				52	w					51	vw		Lattice modes
										35	vw		

[a] ν_i' refer to the near-*cis* conformer.

Table 4
Observed infrared and Raman frequencies (cm^{-1}) and assignments for $CD_3N(D)P(S)F_2$ (abbreviations used: v, very; S, strong; m, moderate; w, weak; br, broad; sh, shoulder; p, polarized; R, Q and P refer to band contours in the gas phase infrared spectrum)

Infrared						Raman							Assignments
Gas	Rel. int.	Amorphous	Rel. int.	Crystalline	Rel. int.	Liquid	Rel. int.	Amorphous	Rel. int.	Crystalline	Rel. int.	ν_i[a]	
				3395	m					3395	vw		crystal effect (d_3)
3482	w	3330	m	3329	s			3332	vw	3325	vw		NH stretch (d_3)
3446	vw												NH stretch (d_3, near-cis)
										3016	vw		
										2995	vw		
2972	vw			2975	vw	2971	p vw	2983	sh	2975	vw		
								2958	vw				
								2841	vw				
				2538	m					2537	vw		crystal effect
2587	rn	2510	rn	2500	s	2520	w	2512	w	2496	vw	ν_1	ND stretch
2564	sh											ν'_1	ND stretch (near-cis)
				2454	sh					2454	vw		Fermi resonance
		2433	m	2425	m	2429	vw	2432	vw	2422	vw		
2265	sh	2255	sh	2259	vw					2260	m	ν_2	CD_3 antisymmetric stretch
				2253	vw					2254	w		
2243	w	2243	w	2243	vw	2249	vw	2248	w	2245	vw	ν_{16}	CD_3 antisymmetric stretch
2237	sh	2223	vw	2222	vw	2226	p vw	2223	vw	2224	vw		Fermi resonance
						2196	vw	(2190)					
2142	w	2135	vw	2135	vw	2135	p w	2134	w	2136	w		Fermi resonance
		2113		2115	vw			2115	vw	2116	vw		Fermi resonance
2100 R													
2094 Q	rn	2085	rn	2087	m	2088	p rn	2086	m	2087	rn	ν_3	CD_3 symmetric stretch
2089 P													
				1389	w								crystal effect (d_3)
1386 R													
1382 Q	m	1392	w	1372	m								NH deformation (d_3)
1376 P													
1230	vs	1240	vs	1240	vs	1237	vw	1237	wvw			ν_8	CN stretch
				1235	sh								
		1125	m	1123	m								
1138 R													
1133 Q	w	1108	m	1115	s	1107	p vw	1107	vw	1107	vw	ν_5	CD_3 symmetric deformation
1126 P													
		1100	sh	1100	sh								
1081	w	1062	vw	1065	vw	1065	sh	1063	vw	1064	vw	ν_4	CD_3 antisymmetric deformation
		1055	vw	1052	vw	1061	vw	1056	vw	1056	vw	ν_{17}	CD_3 antisymmetric deformation
975	s	969	s	971	vs	970	p vw	968	w	970	vw	ν_7	CD_3 rock

Table 4 (*continued*)

Infrared						Raman						Assignments	
Gas	Rel. int.	Amorphous	Rel. int.	Crystalline	Rel. int.	Liquid	Rel. int.	Amorphous	Rel. int.	Crystalline	Rel. int.	ν_i[a]	
940	vs	927	vs	931	s	930	p vw	928	vw	936	vw	ν_9	PF_2 symmetric stretch
				924	s					921	vw		
		895	m	894	s					895	vw		
875	vs			873	vs	874	vw	880	vw	882	vw	ν_{19}	PF_2 antisymmetric stretch
				856	vs	859	vw	859	vw	860	vw	ν_{18}	CD_3 rock
852 Q	s	853	vs	851						849	vw	ν_6	ND deformation
848 P				845	s					849	vw		
805 R													
801 Q	vs	800	s	801	s	792	p vw	793	vw	801	vw	ν_{10}	NP stretch
				786	s					784	vw		crystal effect
				682	vw								crystal effect (d_3)
				678	vw			680	vw	682	vw		PS stretch (d_3)
				669	m								crystal effect
				666	vs					665	m		crystal effect
676 R													
671 Q	m	664	s	660	vs	664	p vs;	661	vs	659	vs	ν_{11}	PS stretch
666 P													
643 R													
637 Q	Vw	627	vw			630	p s	628	vw			ν'_{11}	PS stretch (near-*cis*)
453 R													
449 Q	Vs	445	vs	444	s	444	p m	443	m	444	m	ν_{12}	PF_2 wag
443 P													
415 Q													
410 Q	S	417	vs	417	vs	414	p m	415	m	415	m	ν_{13}	PF_2 symmetric deformation
392 R													
386 Q	S											ν'_{20}	PF_2 rock (near-*cis*)
		388	m	388	m			390	vw	387	vw	ν_{21}	ND out-of-plane bend
382 Q		380	m	370	m	381	ww					ν_{20}	PF_2 rock
				365	sh								
332	Vw	330	br m	331	s							ν_{21}	ND out-of-plane bend
286 Q	M	290	s	290	s	287	w	287	m	289	m	ν_{14}	CNP bend
282 Q	M											ν'_{21}	ND out-of-plane bend (near-*cis*)
		247	w	247	m	252	vw	253	w	247	w	ν_{22}	PF_2 twist
214 br	W											ν'_{22}	PF_2 twist (near-*cis*)
						182	vw					ν'_{14}	CNP bend (near-*cis*)
		170	w	170	vw	170	vw	170	vw	168	vw	ν_{15}	NPS bend
				105	m					117	sh	ν_{23}	CD_3 torsion

Table 4 (*continued*)

Infrared						Raman							Assignments
Gas	Rel. int.	Amorphous	Rel. int.	Crystalline	Rel. int.	Liquid	Rel. int.	Amorphous	Rel. int.	Crystalline	Rel. int.	ν_i [a]	
		90	w	93	vw					95	vw	ν_{24}	asymmetric torsion
				68	vw					83	vw		
				50	m					50	vw		lattice modes
										33	vw		

[a] ν_i' refer to the near-*cis* conformer.

Table 5
Ab initio structure (bond lengths in Å, bond angles in degrees, rotational constants in MHz and dipole moments in debyes) obtained for the near-*trans* and near-*cis* conformers of methylaminothiophosphoryl difluoride

Parameters	RHF/6-31G(d)		MP2/6-31G(d)		B3LYP/6-31G(d)		MP2/6-311+G(d,p)	
	Near-*trans*	Near-*cis*	Near-*trans*	Near-*cis*	Near-*trans*	Near-*cis*	Near-*trans*	Near-*cis*
R(C–N)	1.460	1.460	1.464	1.463	1.467	1.464	1.464	1.464
R(P–N)	1.621	1.624	1.638	1.640	1.647	1.646	1.635	1.637
R(P=S)	1.900	1.899	1.891	1.891	1.912	1.912	1.887	1.887
$r(P–F_1)$	1.556	1.558	1.593	1.594	1.594	1.594	1.593	1.594
$r(P–F_2)$	1.553	1.552	1.587	1.586	1.588	1.588	1.586	1.584
$r(N–H_1)$	0.997	1.000	1.013	1.016	1.012	1.015	1.010	1.012
$r(C–H_2)$	1.081	1.079	1.090	1.089	1.093	1.091	1.090	1.090
$r(C–H_3)$	1.083	1.084	1.093	1.094	1.096	1.096	1.093	1.094
$r(C–H_4)$	1.081	1.081	1.090	1.091	1.092	1.094	1.090	1.090
∠CNP	125.0	126.4	123.2	124.0	124.1	125.6	124.0	123.6
∠NPS	117.4	119.0	117.4	118.3	117.0	118.5	118.3	118.7
$\angle F_1PS$	115.7	114.3	116.4	114.9	116.2	115.0	115.8	114.4
$\angle F_2PS$	116.5	117.0	117.4	118.1	117.3	117.6	117.2	117.8
$\angle H_1NP$	115.5	115.5	114.7	115.5	114.2	115.8	114.5	115.6
$\angle H_2CN$	108.8	109.4	108.7	108.5	108.8	108.8	108.6	108.9
$\angle H_3CN$	111.8	111.8	112.4	112.4	112.6	112.1	112.4	112.5
$\angle H_4CN$	109.6	108.6	108.8	108.7	109.1	109.2	109.2	108.4
τ(SPNC)	174.8	27.0	172.8	31.6	173.0	24.5	173.9	33.1
$\tau(F_1PSN)$	125.0	126.7	125.4	127.3	125.5	126.9	125.8	127.0
$\tau(F_2PSN)$	−123.3	−122.0	−122.4	−120.9	−122.2	−121.5	−122.4	−121.2
$\tau(H_1NPS)$	12.3	188.8	18.3	187.0	18.1	186.4	20.0	185.8
$\tau(H_2CNP)$	154.9	−31.6	159.5	−34.7	159.7	−25.8	159.2	−40.6
$\tau(H_3CNP)$	275.8	89.4	281.0	86.1	281.0	94.7	280.6	80.5
$\tau(H_4CNP)$	37.0	−150.0	42.0	−152.6	42.2	−144.0	41.7	−158.4
$\lvert\mu_a\rvert$	4.724	4.584	4.308	4.399	4.057	4.057	3.430	4.386
$\lvert\mu_b\rvert$	1.656	1.611	1.892	1.436	1.718	1.462	2.179	0.770
$\lvert\mu_c\rvert$	0.253	0.024	0.431	0.046	0.390	0.008	0.432	0.027
$\lvert\mu_t\rvert$	5.012	4.858	4.725	4.628	4.423	4.312	4.514	4.453
A	3830	2656	3743	2585	3691	2558	3772	2600
B	1757	2258	1742	2254	1722	2228	1735	2251
C	1605	1642	1598	1637	1574	1609	1597	1643
$-(E + 1031)$	0.852492	0.850438	1.755879	1.754419	3.578564	3.577259	2.290805	2.289042
ΔE (cm^{-1})		451		320		286		387

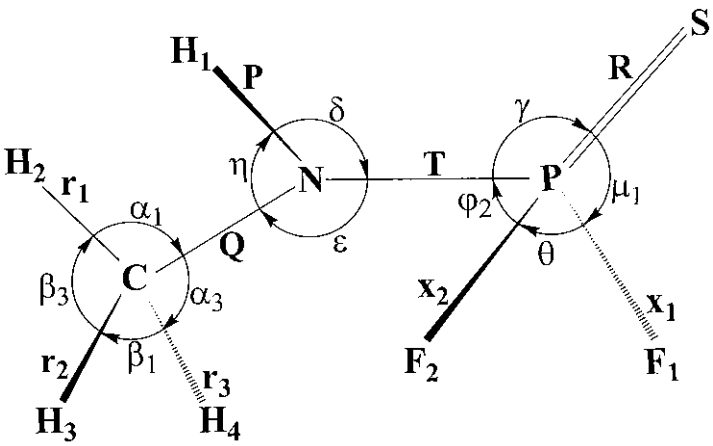

Fig. 14. Internal coordinates of methylaminothiophosphoryl difluoride.

shown in Fig. 18, and, in spite of the crystal field splitting, it is clear that it is the high frequency ν(P=S) which remains in this phase. This shows that in the crystalline solid, the compound has the *trans* conformation.

5. Vibrational assignment

The *trans* conformer of methylaminothiophosphoryl difluoride has a plane of symmetry that coincides with the plane formed by the *a* and *b*

Table 6
Symmetry coordinates for $CH_3N(H)PSF_2$

Species	Description[a]	Symmetry coordinates
A′	NH stretch	$S_1 = P$
	CH_3 antisymmetric stretch	$S_2 = 2r_1 - r_2 - r_3$
	CH_3 symmetric stretch	$S_3 = r_1 + r_2 + r_3$
	CH_3 antisymmetric deformation	$S_4 = 2\beta_1 - \beta_2 - \beta_3$
	CH_3 symmetric deformation	$S_5 = \beta_1 + \beta_2 + \beta_3 - \alpha_1 - \alpha_2 - \alpha_3$
	NH deformation	$S_6 = \eta - \delta$
	CH_3 rock	$S_7 = 2\alpha_1 - \alpha_2 - \alpha_3$
	CN stretch	$S_8 = Q$
	PF_2 symmetric stretch	$S_9 = X_1 + X_2$
	NP stretch	$S_{10} = T$
	PS stretch	$S_{11} = R$
	PF_2 wag	$S_{12} = \mu_1 + \mu_2 - \phi_1 - \phi_2$
	PF_2 symmetric deformation	$S_{13} = 4\theta - \mu_1 - \mu_2 - \phi_1 - \phi_2$
	CNP bend	$S_{14} = \epsilon$
	NPS bend	$S_{15} = r$
A″	CH_3 antisymmetric stretch	$S_{16} = r_2 - r_3$
	CH_3 antisymmetric deformation	$S_{17} = \beta_2 - \beta_3$
	CH_3 rock	$S_{18} = \alpha_2 - \alpha_3$
	PF_2 antisymmetric stretch	$S_{19} = X_1 - X_2$
	PF_2 rock	$S_{20} = \mu_1 + \phi_1 - \mu_2 - \phi_2$
	PF_2 twist	$S_{21} = \mu_1 - \mu_2 - \phi_1 + \phi_2$
	CH_3 torsion	$S_{22} = \tau_1$
	asymmetric torsion	$S_{23} = \tau_2$

[a] Not normalized.

Table 7
Observed and calculated frequencies (cm^{-1}) and potential energy distributions for methylaminothiophosphoryl difluoride

	Vib. no.	Description[a]	*trans*							Near-*cis*						
			Ab initio[a]	Fixed scaled[b]	IR int.	Raman act.	Calc. dep.	Obs.[c]	PED	Ab initio[a]	Fixed scaled[b]	IR int.	Raman act.	Calc. dep.	Obs.[c]	PED
A′	ν_1	NH stretch	3682	3493	84.7	36.0	0.24	3480	$100S_1$	3609	3424	60.3	118.2	0.27	3446	$100S_1$
	ν_2	CH_3 antisymmetric stretch	3235	3034	7.6	71.6	0.69	3023	$99S_2$	3242	3041	4.2	29.4	0.73		$92S_2$
	ν_3	CH_3 symmetric stretch	3122	2929	34.5	107.6	0.00	2963	$99S_3$	3116	2923	37.7	109.0	0.06	2909*	$93S_3$
	ν_4	CH_3 antisymmetric deformation	1585	1504	18.2	14.7	0.75	(1477)	$89S_4$	1580	1499	8.3	20.9	0.67		$73S_4,10S_7$
	ν_5	CH_3 symmetric deformation	1516	1439	1.0	8.7	0.60	(1438)	$100S_5$	1516	1438	1.7	6.9	0.74		$96S_5$
	ν_6	NH deformation	1453	1379	141.7	0.7	0.51	1391	$77S_6$	1472	1397	69.3	2.0	0.70		$69S_6,10S_7$
	ν_7	CH_3 rock	1201	1143	145.3	4.1	0.34	1113	$39S_8,48S_7$	1164	1106	60.2	3.0	0.75		$37S_7,26S_6,14S_8,14S_{10}$
	ν_8	CN stretch	1161	1101	63.7	0.9	0.73	1160	$25S_7,30S_8,$ $22S_{10},21S_6$	1178	1119	94.8	2.7	0.64		$47S_8,29S_7,11S_{18}$
	ν_9	PF_2 symmetric stretch	952	907	281.3	0.7	0.23	923	$66S_9,16S_{11}$	952	907	323.0	2.8	0.28		$44S_9,26S_{11}$
	ν_{10}	NP stretch	901	857	138.8	2.8	0.18	867	$47S_{10},22S_8,$ $20S_{11}$	906	863	163.3	1.6	0.73		$42S_{10},28S_9,13S_8$
	ν_{11}	PS stretch	702	673	40.7	14.4	0.06	699	$36S_{11},31S_9,$ $12S_{12}$	660	627	11.2	20.7	0.06	651	$59S_{11},19S_9,14S_{10}$
	ν_{12}	PF_2 wag	469	460	15.4	9.5	0.27	461	$45S_{12},25S_{11},$ $19S_{14}$	381	379	34.4	3.4	0.73	392	$58S_{12},25S_{13}$
	ν_{13}	PF_2 symmetric deformation	399	398	15.8	4.6	0.53	(378)	$80S_{13},12S_{15}$	367	364	17.1	2.4	0.53		$31S_{13},25S_{20},22S_{12}$
	ν_{14}	CNP bend	299	297	13.0	4.5	0.69	299	$24S_{14},32S_{12},$ $26S_{15},11S_{13}$	448	438	66.8	3.6	0.65	440	$16S_{14},36S_{24},26S_{20}$
	ν_{15}	NPS bend	174	173	0.4	1.5	0.74	(180)	$48S_{15},40S_{14}$	199	197	2.3	2.2	0.74	194*	$46S_{15},32S_{14}$
A″	ν_{16}	CH_3 antisymmetric stretch	3209	3011	11.9	51.8	0.75	(2999)	$100S_{16}$	3206	3007	15.7	72.8	0.67		$89S_{16}$
	ν_{17}	CH_3 antisymmetric deformation	1547	1468	8.3	20.3	0.75	(1452)	$93S_{17}$	1560	1480	10.5	16.7	0.70		$78S_{17},11S_4$
	ν_{18}	CH_3 rock	1192	1131	0.0	3.5	0.75	(1124)	$92S_{18}$	1189	1129	12.2	4.1	0.64		$81S_{18}$
	ν_{19}	PF_2 antisymmetric stretch	906	861	159.2	0.8	0.75	877	$95S_{19}$	905	861	181.9	1.0	0.71		$87S_{19}$
	ν_{20}	PF_2 rock	409	408	1.6	2.4	0.75	414	$70S_{20}$	326	324	2.7	2.2	0.69	325	$39S_{20},20S_{13},10S_{15}$
	ν_{21}	NH out-of-plane bend	377	358	77.8	0.83	0.75	(350)	$35S_{21},36S_{20},16S_{13}$	514	486	81.3	1.69	0.74		$53S_{21},14S_{14},14S_{15}$
	ν_{22}	PF_2 twist	280	278	17.9	3.6	0.75	(253)	$63S_{22},10S_{24}$	233	232	9.6	3.5	0.75	233	$82S_{21}$
	ν_{23}	CH_3 torsion	121	116	25.5	0.8	0.75	(135)	$78S_{23},18S_{24}$	110	105	1.5	0.5	0.60		$87S_{22}$
	ν_{24}	asymmetric torsion	70	70	3.0	0.1	0.75	(112)	$68S_{24},18S_{22}$	73	73	0.8	0.3	0.75		$100S_{23}$

[a] For convenience, the vibrations are ordered according to the *trans* conformer.
[b] Scaled ab initio calculations with factors of 0.88 for C–H stretches, 0.9 for C–H bends, CH_3 torsion and other stretches, 1.0 for heavy atom bends and asymmetric torsion.
[c] Wavenumbers in parenthesis are taken from the infrared or Raman spectrum of the solid, except the one indicated with an asterisk from the Raman spectrum of the liquid.

Table 8
Observed and calculated frequencies (cm^{-1}) and potential energy distributions for methylaminothiophosphoryl difluoride-d_3

	Vib. no.	Description[a]	*trans*							Near-*cis*						
			Ab initio[a]	Fixed scaled[b]	IR int.	Raman act.	Calc. dep.	obs.[c]	PED	Ab initio[a]	Fixed scaled[b]	IR int.	Raman act.	Calc. dep.	obs.[c]	PED
A′	ν_1	NH stretch	3682	3493	85.2	36.0	0.24	3482	$100S_1$	3609	3424	60.4	119.0	0.27	3447	$100S_1$
	ν_2	CD_3 antisymmetric stretch	2401	2253	4.7	35.7	0.71	2265	$99S_2$	2406	2257	2.9	16.7	0.69		$91S_2$
	ν_3	CD_3 symmetric stretch	2240	2101	26.1	52.8	0.00	2093	$99S_3$	2237	2098	25.7	53.3	0.04		$98S_3$
	ν_4	CD_3 antisymmetric deformation	1141	1083	19.0	5.4	0.75	1082	$89S_4,11S_5$	1142	1083	44.9	4.3	0.73		$55S_4,14S1_7,10S_5$
	ν_5	CD_3 symmetric deformation	1197	1136	95.4	0.8	0.20	1133	$40S_5,45S_8$	1121	1064	32.5	9.7	0.64		$16S_5,42S_4,28S_{17}$
	ν_6	NH deformation	1440	1367	171.2	0.8	0.26	1382	$83S_6$	1450	1376	86.1	4.3	0.69		$81S_6$
	ν_7	CD_3 rock	1005	961	93.9	3.9	0.38	973	$38S_7,13S_{14},11S_{10}$	1004	961	178.4	2.0	0.60		$29S_7,11S_5,11S_{14}$
	ν_8	CN stretch	1131	1073	83.3	3.6	0.72	1082	$16S_8,35S_5,28S_{10},12S_4$	1199	1138	44.0	0.7	0.66		$44S_8,45S_5$
	ν_9	PF_2 symmetric stretch	938	891	230.5	2.7	0.01	913	$55S_9,25S_{11}$	935	888	166.2	1.5	0.30		$61S_9,10S_{11}$
	ν_{10}	NP stretch	834	794	105.6	1.1	0.73	805	$22S_{10},26S_7,16S_8,15S_{11}$	830	790	136.2	4.2	0.75		$20S_{10},39S_7,14S_{11}$
	ν_{11}	PS stretch	682	651	22.2	14.6	0.07	677	$33S_{11},25S_9,13S_7,12S_{10}$	650	618	5.0	20.3	0.06	646	$53S_{11},18S_{10},18S_9$
	ν_{12}	PF_2 wag	455	447	18.2	8.7	0.31	449	$52S_{12},22S_{11},15S_{14}$	376	374	36.2	3.5	0.74	386	$69S_{12},14S_{13}$
	ν_{13}	PF_2 symmetric deformation	398	397	15.2	4.6	0.52	(375)	$81S_{13},12S_{15}$	364	361	12.6	2.2	0.53		$31S_{13},34S_{20},12S_{12}$
	ν_{14}	CNP bend	288	286	10.6	4.6	0.67	288	$31S_{15},26S_{12},22S_{14},11S_{13}$	436	428	48.1	4.1	0.65		$15S_{14},25S_{24},24S_{20},14S_{13},12S_{15}$
	ν_{15}	NPS bend	162	161	0.6	1.3	0.74	(169)	$45S_{14},44S_{15}$	182	180	3.0	1.9	0.73	181*	$42S_{15},42S_{14}$
A″	ν_{16}	CD_3 antisymmetric stretch	2383	2236	8.2	26.9	0.75	2241	$99S_{16}$	2379	2232	10.8	35.9	0.73		$90S_{16}$
	ν_{17}	CD_3 antisymmetric deformation	1116	1058	2.9	8.7	0.75	(1065)	$98S_{17}$	1124	1066	38.3	4.1	0.74		$56S_{17},14S_{10},13S_5,10S_8$
	ν_{18}	CD_3 rock	922	875	2.3	3.5	0.75	(859)	$93S_{18}$	915	868	14.7	3.6	0.59		$90S_{18}$
	ν_{19}	PF_2 antisymmetric stretch	905	861	157.5	0.7	0.75	876	$92S_{19}$	905	861	174.0	0.9	0.65		$88S_{19}$
	ν_{20}	PF_2 rock	403	402	1.4	2.3	0.75	414	$71S_{20},12S_{21}$	320	318	2.8	2.2	0.69		$30S_{20},25S_{13},14S_{15},11S_{14}$
	ν_{21}	ND out-of-plane bend	374	355	77.8	0.83	0.75	(347)	$34S_{21},42S_{20},12S_{13}$	502	475	81.3	1.69	0.74		$62S_{21},11S_{15}$
	ν_{22}	PF_2 twist	278	275	17.1	3.7	0.75	(251)	$66S_{22},21S_{20}$	232	231	10.0	3.4	0.75	233	$82S_{22}$
	ν_{23}	CD_3 torsion	98	93	15.1	0.6	0.75	(122)	$81S_{23},15S_{24}$	81	77	1.0	0.3	0.63		$99S_{23}$
	ν_{24}	asymmetric torsion	63	62	4.5	0.0	0.75	(106)	$61S_{24},15S_{21},13S_{23}$	67	67	0.4	0.2	0.75		$100S_{24}$

[a] For convenience, the vibrations are ordered according to the *trans* conformer.
[b] Scaled ab initio calculations with factors of 0.88 for C–H stretches, 0.9 for C–H bends, CH_3 torsion and other stretches, 1.0 for heavy atom bends and asymmetric torsion.
[c] Wavenumbers in parenthesis are taken from the infrared or Raman spectrum of the solid, except the one indicated with an asterisk from the Raman spectrum of the liquid.

Table 9
Observed and calculated frequencies (cm^{-1}) and potential energy distributions for methylaminothiophosphoryl difluoride-d_1

	Vib. no.	Description[a]	*trans*							Near-*cis*						
			Ab initio[a]	Fixed scaled[b]	IR int.	Raman act.	Calc. dep.	obs.[c]	PED	Ab initio[a]	Fixed scaled[b]	IR int.	Raman act.	Calc. dep.	Obs.[c]	PED
A′	ν_1	ND stretch	2698	2560	54.7	16.5	0.26	2588	$99S_1$	2641	2506	47.3	59.2	0.27	2562	$99S_1$
	ν_2	CH_3 antisymmetric stretch	3235	3034	6.7	72.2	0.68	3024	$99S_2$	3242	3041	3.8	28.9	0.72		$92S_2$
	ν_3	CH_3 symmetric stretch	3122	2929	34.4	107.1	0.00	2965	$99S_3$	3116	2923	37.8	108.2	0.06		$93S_3$
	ν_4	CH_3 antisymmetric deformation	1584	1502	13.2	14.4	0.75	(1474)	$91S_4$	1577	1496	7.5	18.8	0.67		$75S_4,14S_{17}$
	ν_5	CH_3 symmetric deformation	1516	1438	1.1	8.7	0.61	(1439)	$100S_5$	1516	1438	3.0	6.4	0.75		$95S_5$
	ν_6	ND deformation	932	886	116.5	1.1	0.66	878	$26S_6,28S_9 22S_8$	1333	1266	102.5	2.3	0.73		$23S_6,29S_7,21S_8,19S_{10}$
	ν_7	CH_3 rock	1195	1137	129.6	4.3	0.35	1116	$53S_7,34S_8$	1171	1114	86.4	3.5	0.70		$45S_7,39S_8$
	ν_8	CN stretch	1303	1237	228.2	1.3	0.54	1265	$23S_8,25S_{10},24S_6,23S_7$	916	870	119.9	4.4	0.49		$19S_8,28S_6,16S_{19},11S_7,11S_{10}$
	ν_9	PF_2 symmetric stretch	975	927	159.4	1.2	0.08	942	$38S_9,28S_6$	983	936	268.3	0.8	0.27		$32S_9,25S_6,19S_{11}$
	ν_{10}	NP stretch	877	834	136.6	1.6	0.21	844	$43S_{10},22S_{11},21S_6$	891	848	141.3	0.8	0.48		$31S_{10},41S_9,18S_6$
	ν_{11}	PS stretch	698	668	35.8	14.9	0.06	692	$35S_{11},31S_9,11S_{12}$	651	619	7.1	20.9	0.07	643	$58S_{11},17S_{10},17S_9$
	ν_{12}	PF_2 wag	466	457	15.8	9.1	0.28	462	$46S_{12},24S_{11},19S_{14}$	378	376	29.2	3.2	0.69		$45S_{12},32S_{13}$
	ν_{13}	PF_2 symmetric deformation	398	396	15.6	4.4	0.52	412	$81S_{13},12S_{15}$	350	346	21.4	2.7	0.51		$40S_{13},30S_{12},14S_{24},11S_{14}$
	ν_{14}	CNP bend	298	296	12.7	4.5	0.69	300	$32S_{14},25S_{15},25S_{14}$	480	471	11.5	2.4	0.75		$31S_{14},27S_{15},14S_{13}$
	ν_{15}	NPS bend	172	171	0.4	1.5	0.75	(178)	$49S_{15},40S_{14}$	199	197	2.8	2.1	0.74	193*	$44S_{15},32S_{14}$
A″	ν_{16}	CH_3 antisymmetric stretch	3209	3011	11.8	51.8	0.75	(2999)	$100S_{16}$	3206	3007	15.7	72.6	0.67		$89S_{16}$
	ν_{17}	CH_3 antisymmetric deformation	1547	1468	8.4	20.3	0.75	(1453)	$93S_{17}$	1560	1480	11.1	16.8	0.70		$77S_{17},12S_4$
	ν_{18}	CH_3 rock	1188	1127	0.1	3.3	0.75	(1100)	$93S_{18}$	1188	1128	3.6	4.2	0.61		$90S_{18}$
	ν_{19}	PF_2 antisymmetric stretch	906	861	155.4	0.8	0.75	850	$95S_{19}$	904	860	177.3	1.3	0.56		$75S_{19}$
	ν_{20}	PF_2 rock	392	392	9.8	2.2	0.75	(375)	$80S_{20}$	417	409	48.6	3.1	0.71	393	$52S_{20},31S_{24},11S_{21}$
	ν_{21}	ND out-of-plane bend	321	304	77.8	0.83	0.75	(332)	$56S_{21},21S_{12}$	305	290	2.2	1.52	0.73	280	$23S_{21},38S_{20},18S_{22}$
	ν_{22}	PF_2 twist	268	267	6.8	3.4	0.75	(250)	$75S_{22},14S_{20}$	221	218	14.1	2.8	0.74	223	$59S_{22},20S_{24},14S_{15}$
	ν_{23}	CH_3 torsion	118	112	19.7	0.7	0.75	(135)	$70S_{23},24S_{24}$	109	104	2.8	0.5	0.60		$86S_{23}$
	ν_{24}	asymmetric torsion	67	66	2.7	0.1	0.75	(112)	$66S_{24},15S_{22}$	71	71	0.6	0.3	0.75		$100S_{24}$

[a] For convenience, the vibrations are ordered according to the *trans* conformer.
[b] Scaled ab initio calculations with factors of 0.88 for C–H stretches, 0.9 for C–H bends, CH_3 torsion and other stretches, 1.0 for heavy atom bends and asymmetric torsion.
[c] Wavenumbers in parenthesis are taken from the infrared or Raman spectrum of the solid, except the one indicated with an asterisk from the Raman spectrum of the liquid.

Table 10
Observed and calculated frequencies (cm^{-1}) and potential energy distributions for methylaminothiophosphoryl difluoride-d_4

	Vib. no.	Description[a]	*trans*							Near-*cis*						
			Ab initio[a]	Fixed scaled[b]	IR int.	Raman act.	Calc. dep.	Obs.[c]	PED	Ab initio[a]	Fixed scaled[b]	IR int.	Raman act.	Calc. dep.	Obs.[c]	PED
A′	ν_1	ND stretch	2698	2560	54.2	16.7	0.26	2587	$99S_1$	2641	2506	47.1	58.6	0.29	2564	$99S_1$
	ν_2	CD_3 antisymmetric stretch	2401	2253	4.6	35.8	0.71	2265	$99S_2$	2406	2257	2.8	16.8	0.69		$91S_2$
	ν_3	CD_3 symmetric stretch	2240	2101	26.1	52.7	0.00	2094	$99S_3$	2237	2098	25.7	53.3	0.04		$98S_3$
	ν_4	CD_3 antisymmetric deformation	1141	1082	8.6	5.6	0.75	1081	$92S_4$	1136	1078	2.5	6.1	0.69		$69S_4,28S_{17}$
	ν_5	CD_3 symmetric deformation	1170	1110	6.4	2.0	0.60	1133	$76S_5$	1172	1113	7.4	2.1	0.68		$77S_5$
	ν_6	ND deformation	885	840	89.8	1.5	0.13	852	$43S_6,19S_{10},14S_{11},13S_9$	890	846	110.6	1.1	0.29		$27S_6,44S_9,20S_{10}$
	ν_7	CD_3 rock	1021	972	33.4	6.7	0.36	975	$36S_7,27S_8,13S_5,12S_6$	1014	965	17.4	4.7	0.75		$31S_7,30S_8$
	ν_8	CN stretch	1280	1215	333.8	0.6	0.74	1230	$40S_8,30S_{10},24S_6$	1290	1225	175.9	0.7	0.68		$40S_8,26S_{10},25S_6$
	ν_9	PF_2 symmetric stretch	969	924	222.5	0.7	0.12	940	$51S_9,15S_{11},14S_6$	979	934	323.9	1.0	0.11		$33S_9,22S_{11},15S_6$
	ν_{10}	NP stretch	832	792	95.8	1.0	0.70	801	$18S_{10},27S_7,18S_8,13S_{11}$	815	774	90.7	4.6	0.73		$12S_{10},40S_7,14S_6,10S_8$
	ν_{11}	PS stretch	678	648	20.5	15.0	0.07	671	$32S_{11},24S_9,13S_{10},12S_7$	644	612	3.4	20.5	0.06	637	$52S_{11},20S_{10},17S_9$
	ν_{12}	PF_2 wag	452	444	18.6	0.56	0.32	449	$53S_{12},22S_{11},15S_{14}$	373	370	29.4	3.3	0.71		$53S_{12},21S_{13}$
	ν_{13}	PF_2 symmetric deformation	397	395	15.1	4.5	0.51	410	$82S_{13},11S_{15}$	345	341	19.3	2.4	0.51		$42S_{13},22S_{12},17S_{24},12S_{14}$
	ν_{14}	CNP bend	287	284	10.4	4.5	0.67	286	$31S_{15},25S_{12},23S_{14},10S_{13}$	181	180	3.8	1.8	0.73	182*	$42S_{14},39S_{15}$
	ν_{15}	NPS bend	162	160	0.6	1.3	0.74	(168)	$44S_{15},45S_{14}$	462	453	14.8	2.7	0.73		$28S_{15},22S_{13},21S_{14}$
A″	ν_{16}	CD_3 antisymmetric stretch	2383	2236	8.1	26.9	0.75	2243	$99S_{16}$	2379	2232	10.7	35.9	0.73		$90S_{16}$
	ν_{17}	CD_3 antisymmetric deformation	1116	1058	2.7	8.6	0.75	(1052)	$98S_{17}$	1122	1064	3.9	8.0	0.68		$70S_{17},26S_4$
	ν_{18}	CD_3 rock	916	870	0.1	3.3	0.75	(860)	$95S_{18}$	915	868	12.4	3.6	0.59		$90S_{18}$
	ν_{19}	PF_2 antisymmetric stretch	905	861	157.0	0.7	0.75	875	$93S_{19}$	905	861	163.5	0.9	0.74		$90S_{19}$
	ν_{20}	PF_2 rock	388	388	8.9	2.2	0.75	(370)	$81S_{20},12S_{23}$	412	405	44.1	3.4	0.70	386	$53S_{20}$
	ν_{21}	ND out-of-plane bend	316	299	77.8	0.83	0.75	(331)	$69S_{21},14S_{12}$	302	286	2.2	1.52	0.73	282	$21S_{21},33S_{20},21S_{22}$
	ν_{22}	PF_2 twist	267	266	6.7	3.5	0.75	(247)	$77S_{22},13S_{20}$	219	216	14.8	2.7	0.74	214	$58S_{22},21S_{24},16S_{15}$
	ν_{23}	CD_3 torsion	96	92	12.3	0.5	0.75	(117)	$73S_{23},18S_{24}$	81	77	1.0	0.3	0.63		$98S_{23}$
	ν_{24}	asymmetric torsion	60	60	3.8	0.0	0.75	(105)	$59S_{24},14S_{23},12S_{22}$	65	65	0.3	0.2	0.74		$100S_{24}$

[a] For convenience, the vibrations are ordered according to the *trans* conformer.
[b] Scaled ab initio calculations with factors of 0.88 for C–H stretches, 0.9 for C–H bends, CH_3 torsion and other stretches, 1.0 for heavy atom bends and asymmetric torsion.
[c] Wavenumbers in parenthesis are taken from the infrared or Raman spectrum of the solid, except the one indicated with an asterisk from the Raman spectrum of the liquid.

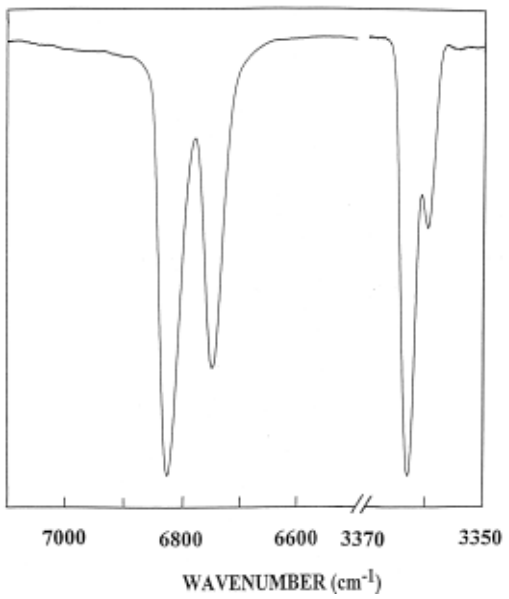

Fig. 15. Fundamental and first overtone bands of ν(N–H) in the mid and near-infrared vapor phase spectra of $CH_3N(H)P(S)F_2$.

principal axes of the molecule and belongs to the C_s point group. Therefore, the vibrations belonging to the A′ block should exhibit A, B or A/B hybrid type infrared band envelopes and polarized Raman lines, whereas the A″ modes should have C-type band contours and depolarized Raman lines. For the near-*cis* conformer which has C_1 symmetry, such distinction between the vibration modes can not be made. Our assignments are also based on isotopic effects. group frequencies and the assignments are supported by the normal coordinate analyses.

Mid-infrared spectra of $CH_3N(H)P(=S)F_2$ and its deuterated species are shown in Figs. 2–5, the far-infrared spectra in Figs. 6–9 and Raman spectra in

Table 11
Directional cosines for the $\partial\vec{\mu}/\partial Q$ of the PS stretch in the principal axis system of $CH_3N(H)P(S)F_2$, $CH_3N(D)P(S)F_2$, $CD_3N(H)P(S)F_2$ and $CD_3N(D)P(S)F_2$

	trans			*cis*		
	$\lvert\cos\alpha\rvert$	$\lvert\cos\beta\rvert$	$\lvert\cos\gamma\rvert$	$\lvert\cos\alpha\rvert$	$\lvert\cos\beta\rvert$	$\lvert\cos\gamma\rvert$
d_0	0.954	0.300	0.000	0.277	0.961	0.000
d_1	0.951	0.309	0.000	0.418	0.908	0.000
d_3	0.944	0.330	0.000	0.152	0.988	0.000
d_4	0.941	0.338	0.000	0.216	0.976	0.000

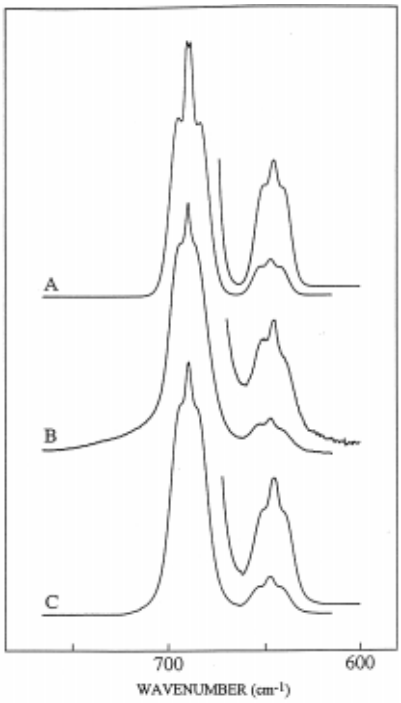

Fig. 16. Comparison of experimental with simulated profiles for the =S stretch: (A) simulation using the near-*cis* and *trans* conformer profiles for the high and low frequency band, respectively; (B) experimental profile; (C) simulation using the *trans* and near-*cis* conformer profiles for the high and low frequency band for $CH_3N(H)P(S)F_2$, respectively.

Figs. 10–13. Observed frequencies are listed in Tables 1–4. In view of the results discussed in the previous paragraph, the fundamentals tabulated and/or discussed below, except where otherwise stated, belong to the *trans* conformer. With the near-*cis* conformer present in the fluid phases, for the latter it is implied that, with a few exceptions where they are observed separately, the near-*cis* fundamentals appear accidentally degenerate with the corresponding *trans* fundamentals. The intense vapor phase infrared band at 3480 cm^{-1} for d_0, and 3482 cm^{-1} for the d_3 derivative, are assigned to the NH stretch of the *trans* conformer, whereas the weaker band at 3446 and 3447 cm^{-1}, respectively, are due to the same fundamental in the near-*cis* conformer. The ND fundamentals of the *trans* rotamer are observed at 2588 cm^{-1} in the d_1 and 2587 cm^{-1} in the d_4 derivative. In both cases, the vapor phase ND stretch shows a low frequency shoulder at 2562 cm^{-1}

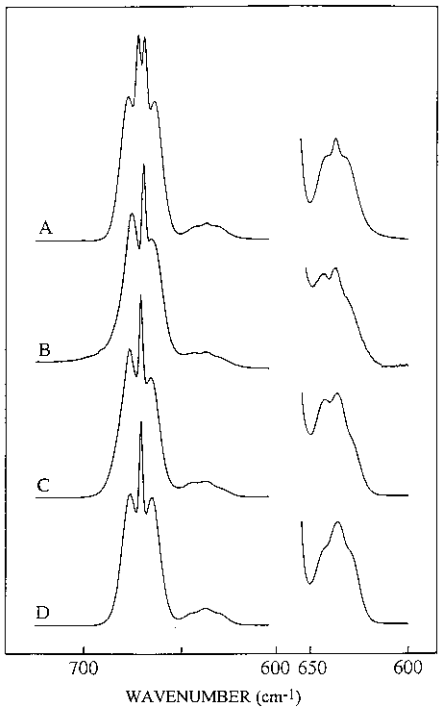

Fig. 17. Comparison of experimental with simulated profiles for the P=S stretch of $CH_3N(D)P(S)F_2$: (A) simulation using the near-*cis* and *trans* conformer profiles for the high and the low frequency band, respectively; (B) experimental profile; (C) simulation using the *trans* conformer profiles of both the d_0 and d_1 derivatives for the high frequency band and the simulation using the near-*cis* conformer profiles of both the d_0 and d_1 derivatives for the low frequency band; (D) simulation using the *trans* and near-*cis* conformer profiles for the high and low frequency band, respectively.

in d_1 and 2564 cm^{-1} in d_4 isotopopomers, respectively, caused by the near-*cis* conformer. In the liquid phase, as shown by the Raman spectra, the N–H stretching mode is observed at substantially lower wavenumber. These shifts can be explained by the existence of hydrogen bonds and the broad band at 3352 cm^{-1} in d_0, and 3357 cm^{-1} in d_3, show a high-frequency shoulder due to the presence of the second conformer. Taking into account the expected H/D shift, the doublet structure of ν(ND) in the Raman spectra of the liquid, at 2534 and 2468 cm^{-1} in d_1 and at 2510 and 2433 cm^{-1} in d_4, cannot be due to the presence of two conformers, but must be due to Fermi resonance between the *trans* ND stretch and an overtone and/or combination band. In the crystalline

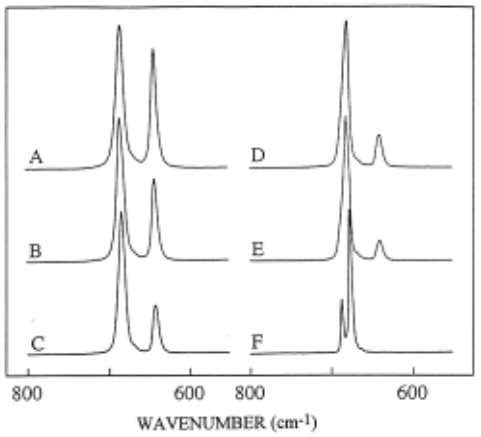

Fig. 18. Raman spectra of the PS doublet (near-*cis* and *trans* conformer) in the liquid phase at 74°C (A); 19°C (B); −35°C (C); −72°C (D); −105°C (E); and the PS stretch in the crystalline phase (F) of $CH_3N(H)P(S)F_2$.

solid, both in the infrared and Raman spectra, a doublet νNX (X = H,D) is observed. This is caused by factor group splitting as a consequence of the presence of two or more molecules in the unit cell of the crystals.

In the CH_3 stretching region of the d_0 and d_3 isotopic species, more than three lines are observed in the Raman spectra of the liquids. Two of these bands at 2844 and 2956 cm^{-1} are intense and strongly polarized and are assigned as a Fermi-doublet of the symmetric CH_3 stretch with the first overtone of the symmetric CH_3 deformation. The shoulder at 2909 cm^{-1} is assigned to the CH_3 stretch of the near-*cis* conformer. The two near degenerate antisymmetric CH_3 stretching motions are assigned to the strongly overlapping, depolarized doublet at 2993 cm^{-1}. Both the infrared and Raman spectra of the crystalline solid show a very complex pattern. The occurrence of crystal site effects in the spectrum of the solid for the NH stretches suggests the possible existence of similar effects for the CH_3 stretches, which contributes to the complexity of the observed pattern. For the d_3 and d_4 species, the CD_3 symmetric stretch is assigned to the strongly polarized Raman line observed at 2087 cm^{-1} in d_3 and at 2088 cm^{-1} in d_4 isotopomer in the spectra of the liquids. The other polarized bands, at 2135 cm^{-1} for d_3, and at 2133 and 2226 cm^{-1} for d_4, are caused by Fermi resonances

Table 12
Temperature intensity ratios of the PS stretch for the conformational stability of liquid methylaminothiophosporyl difluoride and its isotopic derivatives

	T (°C)	$10^4 \cdot (1/T)$, in K^{-1}	$K = I_{trans}/I_{cis}$	ln K
$CH_3N(H)P(=S)F_2$	74	28.80	1.714	0.539
	43	31.65	2.010	0.698
	19	34.20	2.369	0.862
	−10	38.00	3.024	1.107
	−35	42.00	3.697	1.308
	−56	46.10	4.441	1.491
	−72	49.75	5.440	1.694
	−84	52.00	6.253	1.833
	−92	55.25	6.997	1.946
	−105	59.50	8.617	2.154
	−117	64.10	10.629	2.364
	−127	68.50	13.314	2.589
	−138	73.53	18.137	2.898
$CD_3N(H)P(=S)F_2$	70	29.16	1.698	0.529
	43	31.65	1.983	0.685
	17	34.42	2.382	0.868
	−11	38.17	3.072	1.122
	−35	42.02	3.858	1.350
	−55	45.87	4.775	1.563
	−72	49.75	6.159	1.818
	−84	52.91	7.180	1.971
	−92	55.25	8.053	2.086
	−104	59.17	9.247	2.224
$CH_3N(D)P(=S)F_2$	77	28.57	1.756	0.563
	72	28.98	1.879	0.631
	47	31.25	1.989	0.688
	24	33.67	2.560	0.940
	−13	38.46	3.356	1.211
	−38	42.55	4.063	1.402
	−57	46.30	5.166	1.642
	−73	50.00	6.046	1.799
	−83	52.63	6.900	1.932
	−93	55.56	8.355	2.123
	−105	59.52	8.979	2.195
	−115	63.29	10.965	2.395
$CD_3N(D)P(=S)F_2$	69	29.24	1.885	0.634
	46	31.35	2.135	0.758
	26	33.44	2.437	0.891
	−12	38.31	3.351	1.209
	−35	42.02	4.164	1.42G
	−56	46.08	5.099	1.629
	−72	49.73	6.016	1.795
	−83	52.63	6.689	1.900
	−93	55.56	8.001	2.080
	−102	58.48	8.601	2.152
	−111	61.73	11.002	2.405

of the $\nu_s(CD_3)$ with the first overtones and/or combination bands of CD_3 deformations. The antisymmetric A′ and A″ CD_3 stretches of the d_3 and d_4 derivatives are found accidentally degenerate at 2241 and 2249 cm^{-1}, respectively.

The CH_3 symmetric deformation, $\delta_s(CH_3)$, and the CH_3 antisymmetric deformations, $\delta_{as}(CH_3)$ and $\delta'_{as}(CH_3)$ are assigned to the Raman bands observed at 1436, 1470 and 1460 cm^{-1}, respectively, for the liquid. The analogous fundamentals in the d_3 derivative are assigned to the bands at 1114, 1093 and 1063 cm^{-1}. Using the H/D isotope effects, the NX (X = H,D) in-plane bend can be assigned to the bands at 1391 cm^{-1} (d_0), 1382 cm^{-1} (d_3), 878 cm^{-1} (d_1) and 852 cm^{-1} (d_4).

The CH_3 rockings and the CN stretch are expected to occur in the same spectral region [13]. Detailed comparison of the spectra of the different isotopic species allows the two $\rho(CH_3)$ modes to be assigned in the Raman spectra accidentally degenerate at 1107 cm^{-1} in d_0 and at 1113 cm^{-1} in d_1, whereas they split into two bands at 967 and 859 cm^{-1} in the species and 970 and 859 cm^{-1} in d_4. The C–N stretch is observed at 1124 cm^{-1} (d_0), 1265 cm^{-1} (d_1), 1093 cm^{-1} (d_3) and 1230 cm^{-1} (d_4). It may be observed that from d_1 to d_2 and from d_3 to d_4 species this mode is shifted to higher wavenumbers, opposite to what is expected on the basis of the mass effect. This shift must be due to different couplings between the $\rho(CH_3)$ and ν(CN) modes in the different isotopic derivatives.

The PF_2 stretches, $\nu_{as}(PF_2)$ and $\nu_s(PF_2)$ are found to be quite insensitive to deuteration and are assigned to the two most intense infrared bands. The NP stretch can be expected to be sensitive to the deuteration of the N–H bond. Therefore, we assign ν(NP) to the band at 847 cm^{-1} in d_1, and at 792 cm^{-1} in the d_4 compound, whereas the analogous fundamental in the d_0 and d_3 isotopomers occurs almost accidentally degenerate with the antisymmetric PF_2 stretch at 866 and 795 cm^{-1}, respectively.

As mentioned earlier, the extremely strong and polarized Raman doublet at 684 and 640 cm^{-1} are characterized as the PS stretches of the *trans* and near-*cis* conformers, respectively. The CH_3/CD_3 substitution will strongly influence the CH_3 torsional frequency, whereas the N–H out-of-plane deformation will be shifted by deuteration of the N–H bond. Using these arguments, in the Raman spectra of the liquid, the γ(NH) in the d_0 isotope can be assigned at 345 cm^{-1} whereas the τCH_3 in the same isotopomer is assigned at 135 cm^{-1}. As can be expected from the hydrogen bonding in the liquid phase, γ(NH) in the vapor phase occurs some 20 cm^{-1} below the value in the liquid phase. In the spectrum of the solid there appear to be two bands which can be attributed to this mode where it is possible that the higher frequency band is associated with a stronger hydrogen bond. These bonds are found at 390 and 332 cm^{-1}. in the spectrum of the d_1 solid and are only slightly shifted (388 and 331 cm^{-1}) in the spectrum of the crystalline d_4 molecule.

6. Discussion

It should be noted that the description of several of the vibrations in the ‘finger print’ spectral region is rather arbitrary because of extensive mixing as indicated by the PEDs. Also the mixing changes significantly with the isotopic substitution. For example, for the normal species, $CH_3N(H)P(S)F_2$, the NH bend (A′) is a relatively pure mode (77%) at 1391 cm^{-1} with 21% contribution to the 1113 cm^{-1} band. However with deuteration (N-d) it is spread over four bands at 1265 (24%), 942 (28%), 878 (26%) (ND bend) and 844 (21%) cm^{-1} where the relatively strong infrared band at 1265 cm^{-1} assigned as the CN stretch (23%) but it is made up of 23% CH_3 rock, and 25% NP stretch in addition to the 24% contribution from the ND Bend. The CH_3 rock assigned at 1113 cm^{-1} for the “light” species with 48% contribution from this motion and 39% from the CN stretch is only slightly changed to 53% CH_3 rock and 34% CN stretch with its assignment at 1116 cm^{-1} for the N-d molecule. For the “light” compound the PF_2 symmetric stretch at 923 cm^{-1} is 66% this motion and 16% PS stretch whereas the corresponding band at 942 cm^{-1} for the N-d molecule there is now 38% of the PF_2 symmetric stretch and 28% N–D bend. Therefore, the molecular motions for ν_6 through ν_{10} are significantly different for the N-d molecule compared to those for the normal species except for the CH_3 rock.

The enthalpy difference obtained from the Raman spectrum of liquid may differ significantly from that in

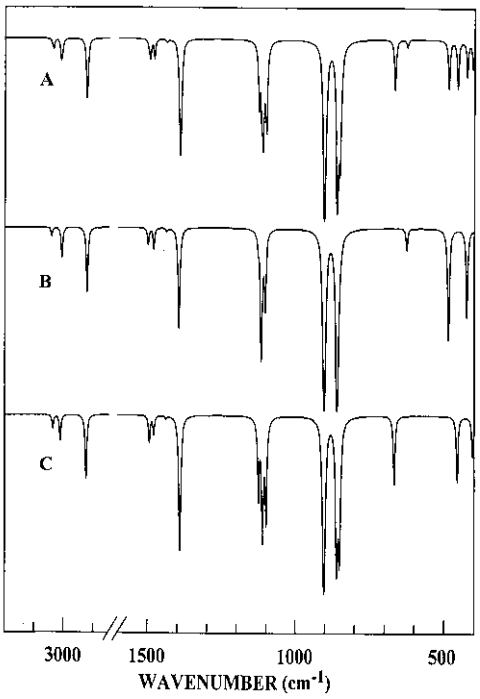

Fig. 19. Calculated infrared spectra of methylaminothiophosphoryl difluoride: (A) mixture of the *trans* and near-*cis* conformers; (B) pure near-*cis*; and (C) pure *trans*.

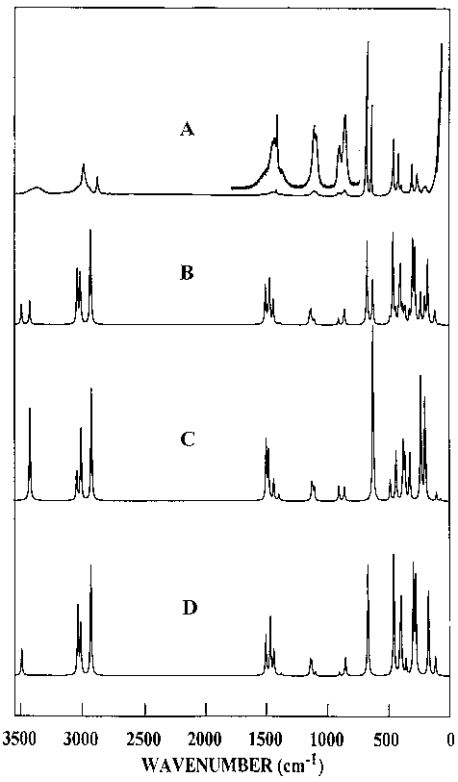

Fig. 20. Comparison of experimental and calculated Raman spectra of methylaminothiophosphoryl difluoride: (A) observed Raman spectrum of the liquid; (B) simulated Raman spectrum of mixture of the *trans* and near-*cis* conformers; (C) simulated Raman spectrum of the pure near-*cis* conformer; and (D) simulated Raman spectrum of the pure *trans* conformer.

the vapor state. However, since both stable conformers have similar dipole moments one does not expect that there will be a change in which conformer is the stable one in the gas, i.e. the *trans* form will be the more stable rotamer in the gaseous phase. This expected result is also supported by the ab initio calculations where the *trans* conformer is predicted to be more stable than the near-*cis* form by the range of 451 cm^{-1} (RHF/6-31G(d)) to 286 cm^{-1} (B3LYP/6-31G(d)). Since these values are relatively large, it is expected that the ab initio calculations predict the correct conformer to be the more stable form.

The uncertainties listed for the enthalpy values are the statistical uncertainties and do not take into account any underlying combination bands or problems with association, etc. In order to minimize such problems it is better to obtain the enthalpy difference from several conformer pairs rather than from just one pair. Nevertheless, one does not expect the error to be more than 15–20% from the Raman data which were taken over a relatively large temperature range so it is clear that the *trans* form is the more stable conformer.

The simulated infrared (Fig. 19) and Raman (Fig. 20) spectra were predicted using fixed scaled wavenumbers and infrared intensities determined from the MP2/6-31G(d) calculations. Infrared intensities were calculated based on the dipole moment derivatives with respect to the Cartesian coordinates. The derivatives were taken from the ab initio calculations transformed to normal coordinates by:

$$\left(\frac{\partial \mu_u}{\partial Q_i}\right) = \sum_j \left(\frac{\partial \mu_u}{\partial X_j}\right) L_{ij}$$

Where Q_i is the ith normal coordinate, X_j is the jth

Cartesian displacement coordinate, and L_{ij} is the transformation matrix between the Cartesian displacement coordinates and normal coordinates. The infrared intensities were then calculated and the predicted infrared spectra of the near-*cis* and *trans* conformers of normal compound are shown in Fig.19B and C, respectively. The mixture of the two conformers is shown in Fig. 19A. These spectra can be compared to the experimental spectra and they provide support for the assignment of the observed bands to the indicated fundamentals, and more importantly, for the identification of the conformer bands. For example, the conformer pair for the PS stretching mode is easily identified from the predicted spectra. Although the PC stretch is predicted too weak and the CH_3 stretch is predicted too strong, the overall simulated infrared spectrum closely resembles the observed spectrum, which provides excellent evidence for the quality of the ab initio calculations.

The evaluation of the Raman activity by using the analytical gradient methods has been developed [27,28]. The activity S_j can be expressed as:

$$S_j = g_j(45\alpha_j^2 + 7\beta_j^2),$$

where g_j is the degeneracy of the vibrational mode j, α_j is the derivative of the isotropic polarizability and β_j is that of the anisotropic polarizability. The Raman scattering cross sections, $\partial\sigma_j/\partial\Omega$, which are proportional to the Raman intensities, can be calculated from the scattering activities and the predicted wavenumbers for each normal mode using the relationship [29,30]:

$$\frac{\partial\sigma_j}{\partial\Omega} = \left(\frac{2^4\pi^4}{45}\right)\left(\frac{(\nu_0 - \nu_j)^4}{1 - \exp\left[\frac{-\mathrm{h}c\nu_j}{\mathrm{k}T}\right]}\right)\left(\frac{\mathrm{h}}{8\pi^2 c\nu_j}\right)S_j,$$

where ν_0 is the exciting wavenumber, ν_j is the vibrational wavenumber of the jth normal mode, and S_j is the corresponding Raman scattering activity. To obtain the polarized Raman scattering cross sections, the polarizabilities are incorporated into S_j by $S_j[(1 - \rho_j)/(1 + \rho_j)]$ where ρ_j is the depolarization ratio of the jth normal mode. The Raman scattering cross sections and calculated fixed wavenumbers are used together with Lorentzian function to obtain the calculated spectra.

The predicted Raman spectra of the *trans* and near-*cis* conformers of the normal compound are shown in Fig. 20D and C, respectively. In Fig. 20B the predicted Raman spectra of the mixtures of the two conformers are shown using the experimentally determined ΔH value of 368 cm^{-1} with the *trans* conformer the more stable rotamer. These spectra should be compared with the experimental Raman spectrum of the liquid which is shown in Fig. 20A. They closely match in both band positions and intensities. Spectroscopic evidence for the conformational stability can be found by this comparison and the conclusion can be drawn that the *trans* conformer is the thermodynamically preferred conformer.

Using scaling factor of 0.88 for carbon–hydrogen stretches, 0.90 for all the other vibrations except 1.0 for the heavy atom bends and asymmetric torsion, the wavenumbers for the fundamentals are predicted from the MP2/6-31G(d) calculations to better than 10 cm^{-1} comparing with the experimental values. These results show that these two scaling factors are sufficient to predict the wavenumbers for the observed fundamentals for these types of molecules. The ab initio predictions for the various isotopomers were valuable in making vibrational assignments for the various deuterated species since it was not possible to obtain the N-d species with high isotopic purity. Additional support for the proposed vibrational assignment was obtained from the Teller–Redlich product rule.

The structural parameters calculated for the two different conformers of $CH_3NHP(S)F_2$ are very similar with major differences being the NPS and CNP angles (Table 5). For the near-*cis* conformer both the CNP and NPS angle are predicted to open by 1–2° which is consistent with the steric interaction of the methyl group with the sulfur atom. However, these differences are not predicted by the MP2/6-311+G(d,p) calculation with the larger basis set. Since the structural parameters are predicted to differ by such a small amount it is not surprising that the force constants for the two conformers also have very small differences which leads to most of the fundamentals for the two conformers to have similar values.

Acknowledgements

The NFWO (Belgium) is thanked for financing

spectroscopic equipment and for travel grants. Prof. Dr. H. Desseyn is thanked for his interest in this work and H. Mulders is thanked for technical assistance. Travel between our two laboratories was provided by a NATO grant. We also acknowledge P. Schilder who recorded some of the earliest vibrational data.

References

[1] J.R. Durig, A.W. Cox Jr., J. Chem. Phys. 63 (1975) 2303.
[2] J.R. Durig, A.W. Cox Jr., J. Chem. Phys. 64 (1976) 1930.
[3] J.R. Durig, A.W. Cox Jr., J. Chem. Phys. 80 (1976) 2493.
[4] J.R. Durig, Y.S. Li, J. Mol. Spectrosc. 70 (1978) 27.
[5] J.R. Durig, B.J. Streusand, Appl. Spectrosc. 34 (1980) 65.
[6] R.L. Odeurs, B.J. van der Veken, M.A. Herman, J.R. Durig, J. Mol. Struct. 117 (1984) 235.
[7] G.H. Pieters, B.J. van der Veken, A.J. Barnes, T.S. Little, J.R. Durig, J. Mol. Struct. 125 (1984) 243.
[8] B.J. van der Veken, R.L. Odeurs, M.A. Herman, J.R. Durig, Spectrochim. Acta 40 (1984) 563.
[9] P. Groner, J.S. Church, Y.S. Li, J.R. Durig, J. Chem. Phys. 82 (1985) 3894.
[10] B.J. van der Veken, P. Coppens, R.D. Johnson, J.R. Durig, J. Chem. Phys. 83 (1985) 1517.
[11] B.J. van der Veken, P. Coppens, R.D. Johnson, J.R. Durig, J. Phys. Chem. 90 (1986) 4537.
[12] B.J. van der Veken, R.S. Sanders, J.R. Durig, J. Mol. Struct. 216 (1990) 113.
[13] J.R. Durig, R.J. Harlan, P. Groner, J. Phys. Chem. 93 (1989) 3041.
[14] B.J. van der Veken, P. Coppens, R.S. Sanders, F.F. Daeyaert, J.R. Durig, J. Mol. Struct. 272 (1992) 305.
[15] B.J. van der Veken, R.S. Sanders, R.J. Harlan, J.R. Durig, Spectrochim. Acta 49A (1993) 1833.
[16] S. Wolfe, Acc. Chem. Res. 5 (1972) 102.
[17] R.G. Cavell, T.L. Charleton, W. Sim, J. Am. Chem. Soc. 93 (1971) 1130.
[18] C. Moller, M.S. Plesset, Phys. Rev. 46 (1934) 618.
[19] F.A. Miller, B.M. Harney, Appl. Spectrosc. 24 (1970) 291.
[20] M.J. Frisch, G.W. Trucks, H.B. Schlegel, G.E. Scuseria, M.A. Robb, J.R. Cheeseman, V.G. Zakrzewski, J.A. Montgomery Jr., R.E. Stratmann, J.C. Burant, S. Dapprich, J.M. Millam, A.D. Daniels, K.N. Kudin, M.C. Strain, O. Farkas, J. Tomasi, V. Barone, M. Cossi, R. Cammi, B. Mennucci, C. Pomelli, C. Adamo, S. Clifford, J. Ochterski, G.A. Petersson, P.Y. Ayala, Q. Cui, K. Morokuma, D.K. Malick, A.D. Rabuck, K. Raghavachari, J.B. Foresman, J. Cioslowski, J.V. Ortiz, B.B. Stefanov, G. Liu, A. Liashenko, P. Piskorz, I. Komaromi, R. Gomperts, R.L. Martin, D.J. Fox, T. Keith, M.A. Al-Laham, C.Y. Peng, A. Nanayakkara, M.W. Wong, J.L. Andres, C. Gonzalez, M. Challacombe, P.M.W. Gill, B. Johnson, W. Chen, M.W. Wong, J.L. Andres, M. Head-Gordon, E.S. Replogle, J.A. Pople, GAUSSIAN 98 (Revision A.6), Gaussian Inc., Pittsburgh, PA, 1998.
[21] P. Pulay, Mol. Phys. 17 (1969) 197.
[22] E.B. Wilson, J.C. Decius, P.C. Cross, Molecular Vibrations, McGraw Hill, New York, 1955.
[23] J.H. Schachtschneider, Vibrational Analysis of Polyatomic Molecules, Parts V and VI, Technical Report Nos. 231 and 57, Shell Development Co., Houston, TX, 1964 and 1965.
[24] G.A. Guirgis, X. Zhu, Z. Yu, J.R. Durig, J. Phys. Chem. 104 (2000) 4383.
[25] B.J. van der Veken, R.S. Sanders, P. Schilder, W. Zhao, J.R. Durig, submitted for publication.
[26] R.L. Odeurs, B.J. van der Veken, M.A. Herman, J. Mol. Struct. 98 (1983) 221.
[27] M.J. Frisch, Y. Yamaguchi, J.F. Gaw, H.F. Schaefer III, J.S. Binkley, J. Chem. Phys. 84 (1986) 531.
[28] R.D. Amos, Chem. Phys. Lett. 124 (1986) 376.
[29] G.W. Chantry, in: A. Anderson (Ed.), The Raman Effect, vol. 1, Marcel Dekker, New York, 1971 (chap. 2).
[30] P.L. Polavarapu, J. Phys. Chem. 94 (1990) 8106.